Front Matter

Full Title

Surface crosslinking of virus-like particles increases resistance to proteases, low pH and mechanical stress for mucosal applications

Short Title

Surface crosslinking of virus-like particles

Authors & Affiliations

Ahmed Ali [a], Suwannee Ganguillet [a], Yagmur Turgay [a], Tim Keys [a], Erika Causa [c], Ricardo Fradique [c], Viviane Lutz-Bueno [d,e], Serge Chesnov [f], Chia-wei Lin [f], Verena Lentsch [a], Jurij Kotar [c], Pietro Cicuta [c], Raffaele Mezzenga [b], Emma Slack [a,*], Milad Radiom [a,b,c,*]

[a] Laboratory of Mucosal Immunology, Institute of Food, Nutrition and Health, ETH Zürich, Zürich, Switzerland
[b] Laboratory of Food and Soft Materials, Institute of Food, Nutrition and Health, ETH Zürich, Zürich, Switzerland
[c] Biological and Soft Systems, Cavendish Laboratory, University of Cambridge, Cambridge CB3 0HE, U.K.
[d] Paul Scherrer Institute PSI, Villigen, Switzerland
[e] Laboratoire Léon Brillouin, CEA-CNRS (UMR-12), CEA Saclay, Université Paris-Saclay, 91191, Gif-sur-Yvette Cedex, France
[f] University of Zürich/ETH Zürich, Functional Genomics Centre Zürich, Zürich, Switzerland

*Milad Radiom (milad.radiom@hest.ethz.ch); Emma Slack (emma.slack@hest.ethz.ch)

Abstract

Virus-like particles (VLPs) are emerging as nano-scaffolds in a variety of biomedical applications including the delivery of vaccine antigens and therapeutic molecules. These soft, colloidal, and proteinaceous structures are nevertheless susceptible to environmental factors such as mechanical stress, proteases and low pH which limit their usefulness, particularly for mucosal applications. We addressed this issue by crosslinking multiple surface sites using polyethylene glycol linkers. Surface crosslinking enhanced the colloidal stability and mechanical strength of VLPs against pH, proteases, and mechanical stresses. Chemical crosslinking thus offers a viable means to enhance resilience of VLPs in mucosal applications.

Teaser

Polyethylene glycol crosslinking virus-like particle (VLP) capsids enhanced the stability and strength of VLPs in mucosal environments.

Keywords

Virus-like particle; Polyethylene glycol; Crosslinking; Force spectroscopy; Human nasal epithelial tissue; Mucus

Introduction

Virus-like particles (VLPs) have emerged as invaluable nano-carriers in biomedical and pharmaceutical applications (*1, 2*). Sensitive cargo, for example proteins, nucleic acids, and drug molecules, can be protected by packaging it inside VLPs. Surface modification of VLPs, with for example antibodies and other chemicals, can also be used to target the cargo to specific cell types. Therefore, in recent years, various therapeutic molecules have been integrated into VLPs for immunotherapy (*3*), gene therapy (*4-6*), chemotherapy (*7-9*), as well as for contrast imaging and photothermal therapy (*10, 11*).

As carriers, VLPs must endure environmental mechanical, physicochemical and biochemical challenges and it is likely that their colloidal properties are an important factor determining their fate (*12*). Key colloidal considerations for “delivery-capable” VLPs include size, colloidal stability, resistance to enzymatic destabilization and mechanical disintegration, target specificity, and responsiveness to stimuli for cargo release. It is important to emphasize these considerations for future developments, as VLPs are characterized as soft (0.1–1 GPa) and proteinaceous colloidal particles (20–200 nm) with immunogenic properties (*12, 13*). Particularly on mucosal surfaces, VLP delivery is faced with challenges associated with the complex physiology of the oral and gastrointestinal routes (*14-16*). Beyond varying pH that may result in a poor colloidal stability, the high concentration of luminal enzymes may digest and destabilize the VLPs, and the thick mucus layer overlaying the epithelium together with mucus flow (e.g., due to mucociliary clearance) may reduce the efficacy of VLPs on mucosal surfaces.

To this end, there is compelling evidence that viruses, viral vectors, and VLPs plastically deform and disintegrate under mechanical force (*17-26*), and disintegrate in unfavorable chemical environments (*27, 28*). For example, we found that VLPs had limited stability in gastrointestinal fluid, restricting their application at mucosal surfaces (this work). This raised the question: can crosslinking VLP capsid enhance the various stability profiles of the VLPs? To address the above question, we employed bifunctional polyethylene glycol (PEG) polymers of appropriate lengths which can tether (or interlace) surface lysine groups of individual coat proteins at the level of single VLPs. Crosslinking VLP capsid via this method was found to enhance the stability and strength profiles of the VLP, opening the possibility for mucosal applications and therefore increasing its application range as outlined below.

76 VLP or viral vector PEGylation, without crosslinking, has been exploited as a means to
77 enhance biological function, especially with adenovirus vectors (Adv). For example,
78 PEGylated Adv (PEG molecular weight, MW 5 kDa) protected the vector from neutralizing
79 antibodies *in vitro*, and increased transgene expression in 'native Adv'-immunized mice
80 (*29*). Similarly, using PEGylated Adv, a prolonged transgene expression and a reduced
81 immune activation against the vector were reported in intratracheal as well as intravenous
82 administrations (i.e., mucosal and systemic routes) in immunized mice (*30, 31*).
83 Subsequent experiments showed a complex dependence of immune protection (or other
84 biological functions) on new particle-level immunobiophysical properties attained after
85 PEGylation (*32-34*). Therefore, for example, conjugation optimization led to reduced anti-
86 vector serum antibody and persistent transgene expression in a mouse model of lung
87 cancer (*35*). In addition to Adv and PEG, other polymer conjugation to other VLPs and
88 plant viruses has been investigated. For example, poly(oligo(ethylene glycol) methyl ether
89 acrylate) (POEGMEA), poly(norbornene-(oligo(ethylene glycol) ester)) (PNB) and
90 poly(methacrylamido glucopyranose) (PMAG) (all ~ 10 kDa) were conjugated to the VLP
91 derived from the bacteriophage Q*β* and showed similar effects to PEG in shielding the
92 VLP from immune recognition (*36, 37*). In other directions, PEG (3.4 kDa) was used to
93 tether a fluorescent molecule to cowpea mosaic virus (CPMV) for intravital vascular
94 imaging (*38*), and PEG (0.6 kDa) to tether folic acid to CPMV for targeting of cancer cell
95 lines (*39*).

96 Our model VLP is assembled from 180 copies of *Acinetobacter* phage coat protein AP205
97 (*26*). AP205 VLP is a versatile VLP platform for conjugation of various antigenic molecules
98 including epitopes from SARS-Cov-2 virus (*26, 40, 41*). The versatility of AP205 VLP is
99 due to its surface exposed N- and C-termini which were genetically modified to carry and
100 present antigenic epitopes on the surface of the VLP (*42*). We investigated the effects of
101 PEG surface crosslinking of AP205 VLP on enzymatic stability, resistance to mechanical
102 force and mucus penetrability. To explore different modes of crosslinking, the AP205 VLP
103 was reacted with homobifunctional – leading to crosslinking – and monofunctional PEG
104 linkers of 0.5–1.4 kDa. We found that PEG-crosslinked AP205 VLPs, but not simply
105 PEGylated VLPs, showed enhanced stability profiles against physicochemical, enzymatic,
106 and mechanical stress. In terms of mucus translocation in *in vitro* 3D human nasal
107 epithelial tissue with mucociliary clearance, PEG-crosslinking did not limit the translocation
108 process. We also examined the induction of anti-PEG antibody responses after
109 subcutaneous injection of PEGylated VLPs (*33, 43, 44*). Consistent with the high

110 immunogenicity of AP205 VLP (*40, 41*), we found specific serum IgG against PEG. The
111 PEG surface crosslinking approach can therefore be employed in diverse VLP mucosal
112 applications by offering a biomedical toolbox that enhances the stability and strength
113 profiles of VLPs. However, this must be restricted to cases where the immune activation
114 to PEG can be tolerated, for example when the latter does not exceed the immune
115 response against the VLP itself or lead to anaphylaxis.

116

117 Results

118 Surface sites crosslinking of native AP205 VLP was performed using PEG crosslinker
119 molecules. Thereby, homobifunctional PEG linkers were reacted with AP205 VLP
120 resulting in PEG-crosslinked AP205 VLPs, named bPEG$_n$-AP205 VLP, where n refers to
121 the number of PEG monomer units. As control, monofunctional PEG molecules were
122 conjugated to AP205 VLP resulting in PEGylated but not PEG-crosslinked AP205 VLPs,
123 named mPEG$_n$-AP205 VLP. The functional group(s) of the PEG molecules was N-
124 hydroxysuccinimide (NHS) ester which reacts with lysine residues and N-terminus of
125 AP205 coat proteins (c.f. **Figure 1**(a)). The sequence of AP205 monomer and the details
126 of the reactive PEG molecules are presented in **S1**. We note that in the conditions used,
127 the crosslinking was between AP205 monomers within individual particles, and we did not
128 observe aggregation between whole particles (**S2**). Transmission electron microscopy
129 (TEM) showed that the VLPs retained their spherical geometry after the conjugation
130 reaction with the linker molecules (**S3**). Furthermore, PEGylation did not detectably alter
131 the size of VLPs for any lengths of PEG crosslinker tested, n = 9–25 (**Fig. S3-1**).

132

133 Crosslinking AP205 VLP capsid using polyethylene glycol (PEG) molecules

134 Investigations with mass spectrometry and reducing SDS-polyacrylamide gel
135 electrophoresis (SDS PAGE) revealed that AP205 VLP reaction with homobifunctional
136 PEG crosslinkers resulted in PEG-crosslinked AP205 dimers, trimers, and possibly higher
137 oligomers. In the representative SDS PAGE shown in **Figure 1**(b), in the lanes associated
138 with bPEG$_n$-AP205 VLPs (n = 9 to 25), bands in MW range 37–50 kDa (marked with purple
139 arrows/circles) correspond to PEG-crosslinked AP205 dimers, and bands in MW range
140 50–75 kDa (marked with orange arrows/pentagons) correspond to PEG-crosslinked

141 AP205 trimers. Furthermore, using nano ultra-performance liquid chromatography
142 coupled to mass spectroscopy, it was found that lysine (K) residues K4 and K61 and K4
143 and K94 were involved in the crosslinking reaction (**Table S4-7**). In **Figure 1**(c), a
144 schematic of PEG linkages between individual AP205 monomers near the three-fold axis
145 of symmetry is shown. Using coordinates from the cryo-electron microscopy
146 reconstruction of the AP205 VLP (5LQP) in Visual Molecular Dynamics (VMD) (*42, 45*),
147 the N-N interatomic distances in K4–K61 linkage were estimated to be 1.8 nm and in K4–
148 K94 linkage to be 1.6 nm and 2.4 nm. Calculation of end-to-end probability distributions of
149 PEG_9, PEG_{17} and PEG_{25} linker molecules using the worm-like chain model are also shown
150 in **Figure 1**(c) (*46*). The calculated extension lengths are consistent with the interatomic
151 distances. In addition, longer crosslinker molecules extend to longer tethering lengths with
152 a higher relative probability. Additional details regarding the mass spectroscopy and SDS
153 PAGE of PEG modified VLPs are found in **S4** and **S5**, respectively. After ensuring an
154 appropriate reaction stoichiometry (**S2**) and to prevent a large excess of free PEG
155 molecules (which is important in subsequent experiments), all reactions were carried out
156 using a 10x molar ratio of crosslinker molecule to AP205 monomer.

157

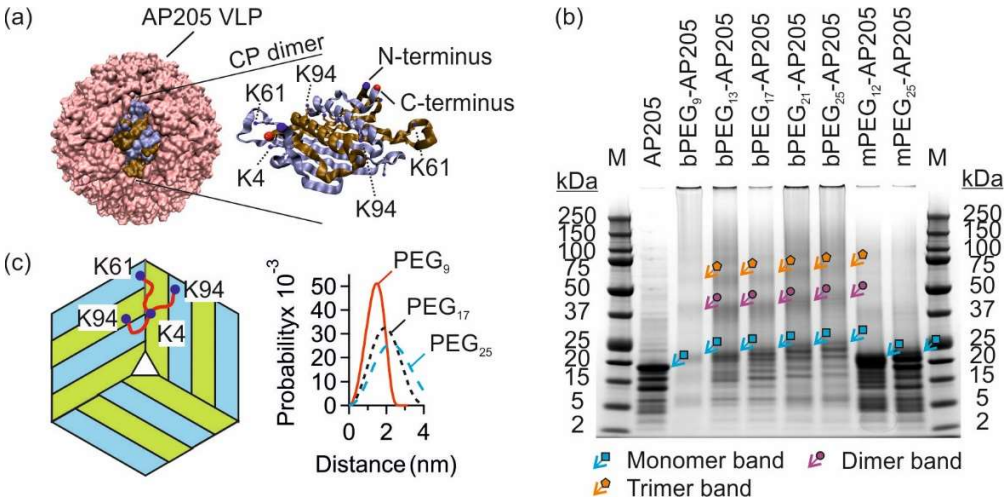

158

159 **Figure 1: Homobifunctional PEG molecules crosslinked individual AP205 coat**
160 **proteins.** (a) Schematic of AP205 virus-like particle (VLP) and AP205 coat protein (CP)
161 dimer (*42*). The N-terminus (blue) of one coat protein, the C-terminus (red) of the
162 neighboring coat protein, together with several lysine residues are marked. (b) Reducing
163 SDS polyacrylamide gel electrophoresis of native AP205 VLP, PEG-crosslinked $bPEG_n$-
164 AP205 VLPs (n = 9–25), and PEGylated but not crosslinked $mPEG_n$-AP205 VLPs (n = 12
165 or 25). M is PageRuler Plus Prestained Protein Ladder. Monomer MW band is marked
166 with cyan arrows/squares, dimer MW band with purple arrows/circles and trimer MW band

167 with orange arrows/pentagons. (c) Schematic of AP205 coat proteins arrangement near
168 the three-fold axis of symmetry and the assignment of PEG-crosslinked lysine residues
169 K4–K61 and K4–K94 from different AP205 monomers. In the schematic, 3 dimers are
170 shown with their monomers colored in blue and green. The end-to-end probability
171 distributions of PEG_n (n = 9, 17 and 25) tethers calculated from an analytical worm-like
172 chain model (*46*).
173

174 **Enhanced colloidal and enzymatic stability of PEG-crosslinked AP205 VLPs**

175 VLPs are potentially interesting scaffolds for the oral or intranasal delivery of biomolecules,
176 requiring stability in pH-varying environments and in the presence of high concentrations
177 of proteases (*1, 2, 12*). Therefore, increasing their stability in the complex mucosal
178 environment is of high translational relevance.

179 Straightforward buffer experiments using dynamic light scattering (DLS) showed that
180 native AP205 VLP was stable at pH 7.4 but aggregated at pH 2.0–6.0 (**Fig. S6-1**). PEG-
181 crosslinking increased the stability of AP205 VLP up to pH ~ 4.0 (**Fig. S6-2**). We then
182 tested the enzymatic stability of PEG-crosslinked AP205 VLPs in pig and mouse gastric
183 fluids. In PBS, an incubation time of 2 h (or longer) at 37°C did not affect the stability or
184 electrophoretic mobility of the VLPs (*26*) (**Figure 2**). In pig gastric fluid, which had a pH of
185 3.0 and high protease concentration, PEG-crosslinked AP205 VLPs, namely $bPEG_9$-
186 AP205 VLP, $bPEG_{17}$-AP205 VLP, and $bPEG_{25}$-AP205 VLP, showed improved stability
187 after 5 min of incubation (i.e., a band, marked with arrow, remained at the expected MW,
188 with fewer breakdown products than the unmodified VLP). At the later time points of 30
189 min, 1 h and 2 h, the intact portion was disintegrated and signs of aggregation
190 (accumulation of material in the wells of the gel) appeared. Interestingly, the PEGylated
191 but not crosslinked AP205 VLP, namely $mPEG_{25}$-AP205 VLP, showed a similar behavior
192 to native AP205 VLP (i.e., it disintegrated in as little as 5 min). This observation indicates
193 that PEG-crosslinking VLP capsid, but not PEGylation per se, is a viable approach to
194 overcome the susceptibility of VLPs to colloidal and enzymatic instability.

195

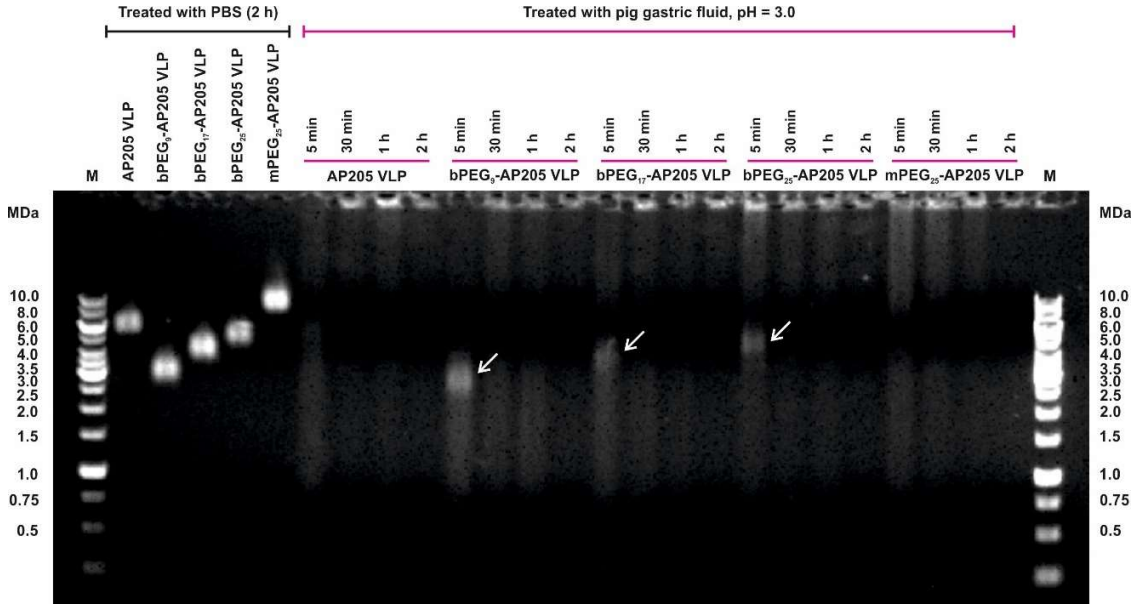

Figure 2: Enhanced enzymatic stability of PEG-crosslinked VLPs in gastric fluid. Agarose gel electrophoresis of AP205 VLP, bPEG$_9$-AP205 VLP, bPEG$_{17}$-AP205 VLP, bPEG$_{25}$-AP205 VLP and mPEG$_{25}$-AP205 VLP in PBS and in pig gastric fluid (pH 3.0), respectively on the left and right of the gel. Incubation times varied between 5 min, 30 min, 1 hour and 2 hours at 37°C. Arrows at time point 5 min indicate persistent PEG-crosslinked AP205 VLPs in gastric fluid. M stands for marker.

The complete data set of the enzymatic stability of PEG-crosslinked VLPs in shown in **S7**. Thereby, experiments in pig gastric fluid at pH 4.7 corroborated the stabilizing effect of PEG-crosslinking, but not simple PEGylation, in the presence of proteases. At this pH, the PEG-crosslinked VLPs were stable at all time points. In pig gastric fluid at pH 5.5, all VLPs were found to be stable over 1 h of incubation. Incubation in mouse gastric fluid at pH 4.6 presented a similar behavior where the PEG-crosslinked AP205 VLPs appeared to be more stable compared to the naked and PEGylated but not crosslinked AP205 VLP.

Enhanced stiffness and strength of PEG-crosslinked AP205 VLPs

Susceptibility to mechanical stress sets a limit on potential applications of VLPs in various indications. This occurs during interactions with cells, e.g. during endocytosis or antigen presentation to B cells, or when exposed to mucus or fecal flow (*47-53*). Therefore, we examined the nanomechanical properties of native and PEG-crosslinked AP205 VLPs using atomic force microscopy (AFM) force-indentation spectroscopy.

The schematic of AFM measurements is depicted in **Figure 3**(a) and details are provided in the methods section. The example shown in **Figure 3**(b) depicts a single representative AP205 VLP for which the height prior to indentation (H_{i}) and after indentation (H_{f}) were evaluated. Generally, application of a single indentation did not significantly change the height of the VLP. This is different from repeated indentations which have been shown to result in virus or VLP disintegration due to fatigue (*17-19, 23-26*). **Figure 3**(c) shows the heights distributions of AP205 VLP with the respective average values.

The force versus indentation distance ($F-\delta$) curve was used to calculate the stiffness, and the force versus indentation time ($F-t$) curve to calculate the strain rate. An example of these curves for the same VLP (**Figure 3**(b)) is shown in **Figure 3**(d). After physical contact was established between the AFM tip and the VLP, the force increased due to the resistance of VLP to mechanical deformation. The linear part of the response was used to calculate the stiffness, $k = dF/d\delta$ and total indentation, $\delta = \Delta F/k$. In the same range, a linear fit to force versus indentation time curve gave the indentation force rate $\dot{F} = dF/dt$, which was converted to strain rate via $\gamma = \dot{F}/k\delta$. After an initial linear response, the VLP yielded at a threshold force.

The histograms of maximal force and maximal indentation (indent.) of AP205 VLP together with the average values of these parameters are shown in **Figure 3**(e). The physical significance of these parameters is that at a force (or indentation) higher than the average maximal force (or indentation), the force response of VLP deviates from a linear behavior. A non-linear behavior is an indication of plastic deformation. After plastic deformation, capsid stiffness diminishes as a result of fatigue (*17-19, 23-26*).

The histograms of stiffness and strain rate of AP205 VLP together with the average values of these parameters are shown in **Figure 3**(f) and (g), respectively. For this VLP, we previously showed that the standard linear solid model (SLSM, **Figure 3**(h)) interprets the stiffness as a function of the strain rate (*26*). In particular, we found that at a strain rate < 100 1/s, the overall mechanical response is governed by k_0 . We thereby found a good agreement between the current evaluation of AP205 stiffness (47±15 pN/nm) with the previous one (53±23 pN/nm) at low strain rates.

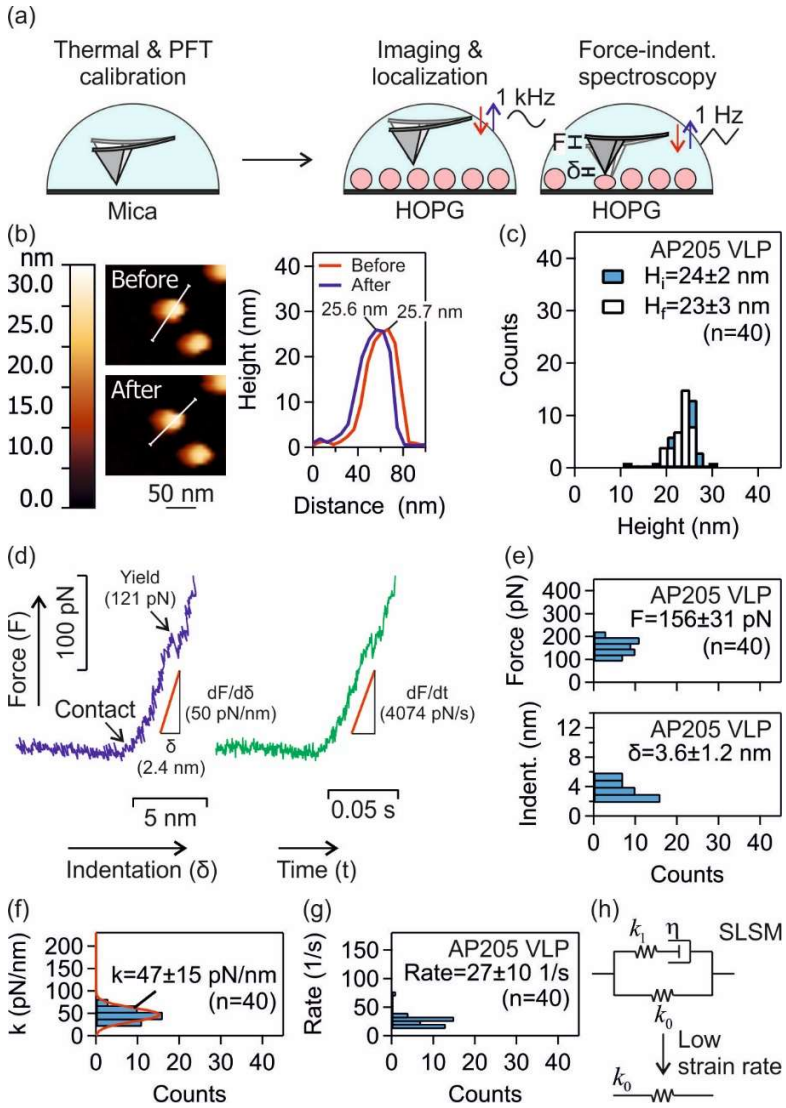

Figure 3: Mechanical properties of AP205 VLP investigated using AFM force-indentation spectroscopy. (a) Schematic of AFM calibration on freshly cleaved mica, and force-indentation spectroscopy of HOPG-immobilized VLPs. Single VLPs were localized using PeakForce tapping imaging (base tapping rate of 1 kHz) prior to force measurements using normal ramp at base approach-retraction rate at 1 Hz. (b) Example of height evaluation for a single AP205 VLP before and after force application. (c) Height distributions of AP205 VLP before and after force measurements. (d) Example of force-indentation distance and force-indentation time curves for AP205 VLP. The linear regime of force-indentation distance response was used to calculate the stiffness. In the same range, a linear fit to force-indentation time response gave the indentation force rate. (e, f and g) Histograms of maximal force and indentation (indent.) (e), stiffness (f) and strain rate (g) of AP205 VLP. Mean ± standard deviation is reported. The number (n) of AP205 VLPs in repeat measurements is indicated. (h) Standard linear solid model (SLSM). At low strain rates, there is no contribution from friction (or rate dependent resistance) to indentation.

265 Similarly, the mechanical properties of PEG-crosslinked AP205 VLPs, namely $bPEG_9$-
266 AP205 VLP, $bPEG_{17}$-AP205 VLP, $bPEG_{25}$-AP205 VLP were evaluated, and the results
267 are shown in **Figure 4**. The initial heights and the heights after a single indentation showed
268 similarity among the native and PEG-crosslinked VLPs. The distributions of maximal force
269 and indentation (indent.) for PEG-crosslinked AP205 VLPs however showed variations
270 compared to native AP205 VLP. The average maximal force (corresponding to strength)
271 was found to be higher and accordingly the average maximal indentation lower compared
272 to native AP205 VLP. The increased (decreased) maximal force (indentation) of PEG-
273 crosslinked AP205 VLPs indicated reduced susceptibility to mechanical perturbation.
274 Finally, the average stiffness for these VLPs was also higher by a factor of 1.3–2.0 than
275 the stiffness of native AP205 VLP at similar range of strain rate.

276

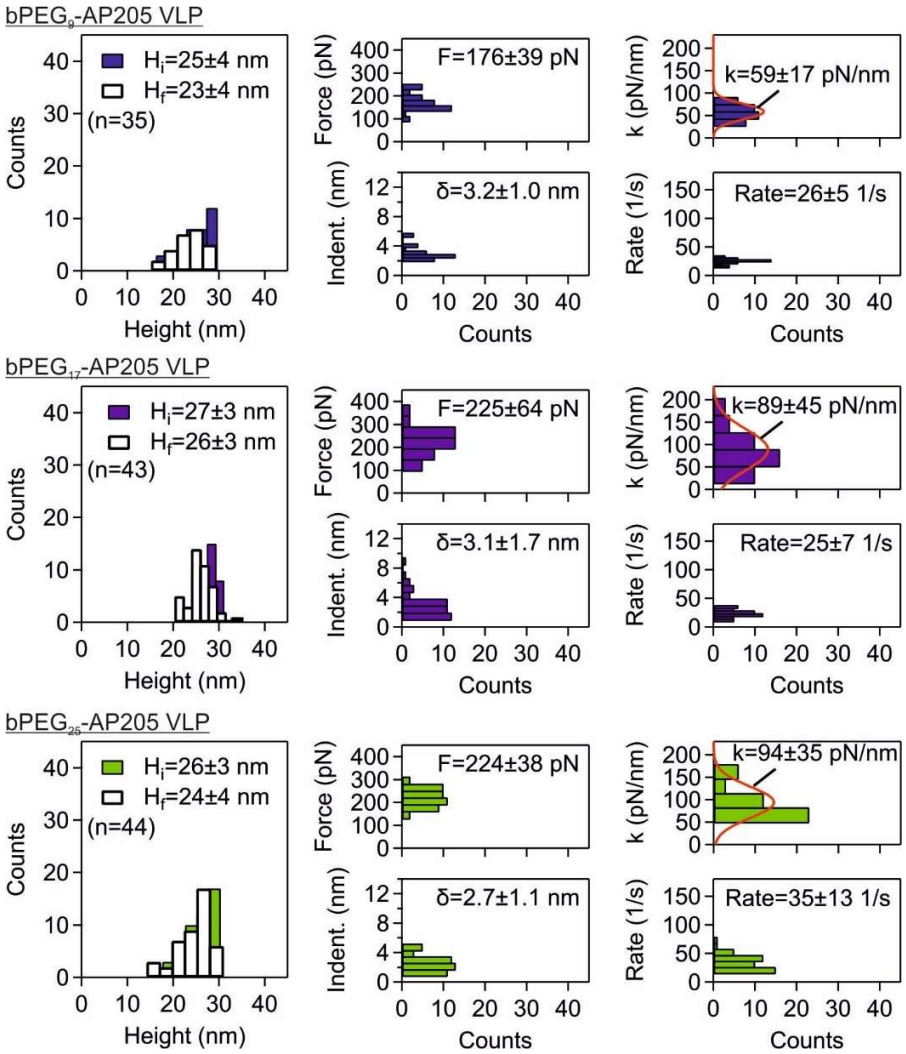

Figure 4: Enhanced strength and stiffness of PEG-crosslinked AP205 VLPs. Mechanical properties of PEG-crosslinked AP205 VLPs, namely bPEG$_9$-AP205 VLP, bPEG$_{17}$-AP205 VLP and bPEG$_{25}$-AP205 VLP, investigated using AFM force-indentation spectroscopy. Distributions of height before and after indentation, maximal force/indentation in linear response regime, and stiffness/strain rate are shown together with mean ± standard deviation. The number (n) of VLPs in repeat measurements is indicated.

Capsid response to indentation is dependent on its size and shell thickness (*54*). We therefore evaluated these geometrical parameters using small angle X-ray scattering (SAXS). In SAXS, the intensity of scattered X-ray, I, is a function of the momentum transfer vector, q. For a spherical core-shell structure in a dilute solution regime, $I(q)$ has an exact analytical solution, which is called the form factor. The X-ray scattering spectra of the native and PEGylated VLPs together with fits to spherical core-shell form

292 factor are shown in **Figure 5**(a). In each case, we find a good agreement between the
293 experimental scattering data and the fit, based on the low values for the fitting error (χ^2).
294 In the summary panel in **Figure 5**(b), it is shown that the diameter (D) and shell thickness
295 (h) of AP205 VLP increased after PEGylation. In addition, while the VLP diameter
296 remained somewhat constant after PEGylation, the shell thickness increased with PEG
297 length and had its highest value for the PEGylated but not crosslinked VLP.

298 Subsequent to the evaluation of stiffness (from AFM) and diameter and shell thickness
299 (from SAXS), the elastic modulus was calculated from the relation $E = Dk/2h^2$ and the
300 results are provided in **Figure 5**(b) (*55, 56*). For AP205 VLP we found an elastic modulus
301 equal to about 89±31 MPa which is slightly smaller than our previous estimation of this
302 parameter, equal to 111±28 MPa (*26*). The difference originates mainly from incorporating
303 a stiffness value in the above relation, equal to 93±23 pN/nm, that was collected at the
304 high strain rate 10^4 1/s. Therefore, the elastic modulus remained somewhat constant
305 among the native and PEG-crosslinked VLPs. This observation can be explained as
306 follows. In nanoindentation experiments, the shell is compressed and bent locally; the shell
307 compression modulus and bending modulus contribute to the effective elastic modulus E
308 (*56-58*). Two-end conjugated PEG tethers disfavor bending because it results in chain
309 stretching, therefore increasing the bending modulus. Reduction in coat protein positive
310 charges after PEG conjugation reduces the inter-atomic repulsion during compression;
311 however, it introduces inter-chain steric repulsion, therefore affecting the compression
312 modulus. These somewhat opposing effects resulted in an unmodulated elastic modulus
313 ~ 90 MPa for the native and PEG-crosslinked VLPs. The higher stiffness of PEG-
314 crosslinked VLPs compared to native VLP is therefore associated with an increase in the
315 shell thickness, as well as stretching two-end conjugated PEG tethers that resist extension
316 in local bending (*59*). The effect of chain stretching becomes evident where the PEGylated
317 but not crosslinked AP205 VLP, namely $mPEG_{25}$-AP205 VLP, was investigated. This VLP
318 showed a lower elastic modulus and stiffness compared to its PEG-crosslinked
319 counterpart, namely $bPEG_{25}$ AP205 VLP (**S8** and **Figure 5**).

320

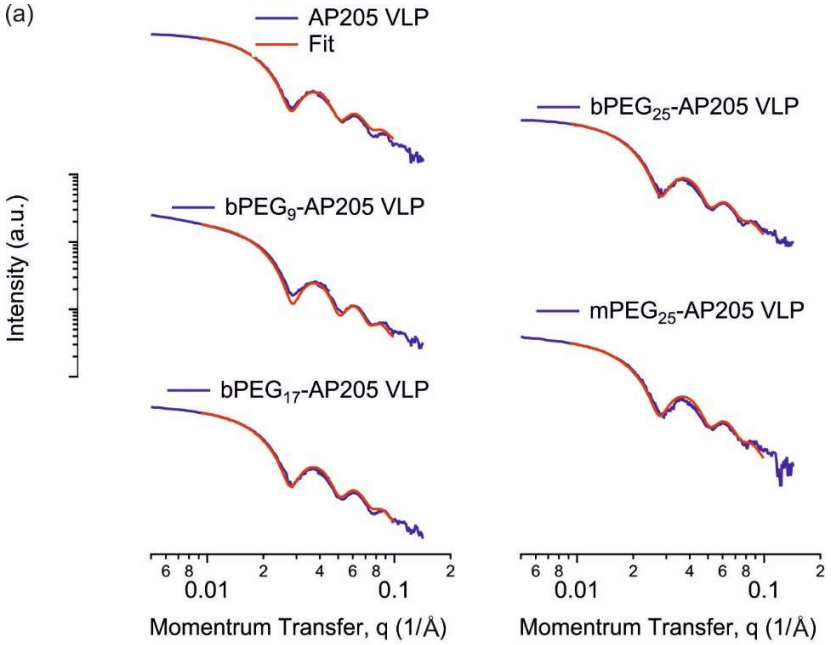

(b)

VLP entry	Stiffness (pN/nm)	Diameter (nm)	Shell thickness (nm)	Elastic modulus (MPa)
AP205	47±15	27.6	2.7	89±28
$bPEG_9$-AP205	59±17	28.8	3.2	83±24
$bPEG_{17}$-AP205	89±45	28.5	3.6	98±49
$bPEG_{25}$-AP205	94±35	28.4	4.0	83±31
$mPEG_{25}$-AP205	76±29	28.8	4.4	57±22

Figure 5: Geometrical and mechanical parameters of native and PEGylated AP205 VLPs. (a) Small angle X-ray scattering (SAXS) spectra of AP205, $bPEG_9$-AP205, $bPEG_{17}$-AP205, $bPEG_{25}$-AP205 and $mPEG_{25}$-AP205 VLPs, together with fits to spherical core-shell form factor. (b) Summary panel of the geometrical and mechanical properties of the VLPs.

PEG-crosslinking does not restrict mucus translocation of AP205 VLP

A major feature of intestinal and respiratory sites where VLP application is relevant is the production of mucus. Mucus is an adhesive, viscoelastic, porous fluid that is characterized with strong electrostatic and hydrophobic interactions due to mucin glycoproteins, a porosity in the range 100–5000 nm, an elastic modulus 2.5 Pa and viscosity 100 Pa s (*60, 61*). Mucus in the airways epithelium is consistently pushed out via mucociliary clearance (*62, 63*). We investigated the effect of PEG-crosslinking on the translocation of AP205 VLPs across mucus against mucociliary clearance. For this purpose, *in vitro* 3D human monodonor nasal epithelial tissues from Epithelix (MucilAir™) were employed. The tissues

337 were characterized as having fully differentiated mucus producing goblet cells, ciliated
338 cells with motile cilia, as well as other cells of normal human nasal epithelial tissue.

339 The schematic of experiments is shown in **Figure 6**(a). The details of the delivery of
340 fluorescently labelled VLPs are provided in the methods section. On delivery of VLP
341 solution from the apical side to the center of the tissue (i.e., position 1 in the schematic),
342 the solution immediately wetted the entire apical area of the tissue. Delivered VLPs then
343 translocated through mucus by diffusion or were transported in flowing mucus in the
344 direction of mucociliary clearance. The lateral distribution and vertical translocation were
345 monitored using laser scanning confocal microscopy (LSCM). In **Figure 6**(b), a
346 representative example of mean fluorescence intensity (MFI) variation with height
347 collected in the center, [0, 0] mm, of tissue 3 prior to VLP delivery (VLP-) and after the
348 delivery of $mPEG_{25}$-AP205 VLP^{GelRed} (VLP+) is shown. In the VLP- case, the location of
349 maximum MFI was at the height level of the semipermeable membrane which was
350 assigned to 0 μm. After VLP delivery, the maximum of MFI shifted to a higher height value
351 (about 40 μm) while the peak associated with semipermeable membrane was still
352 observable. The MFI vs height spectra were normalized by the MFI values at height = 0
353 μm. The normalized MFI (norm. MFI) spectra are also shown in **Figure 6**(b). The
354 normalized MFI spectrum of VLP- was then subtracted from that of VLP+ to give the net
355 MFI spectrum. The net MFI spectra from the center, [0, 0] mm, together with spectra at
356 positions [-1, 0] mm, [+1, 0] mm, [0, -1] mm and [0, +1] mm, are shown in **Figure 6**(c).
357 These spectra provided information about the height location of VLP deposition and the
358 net value of MFI at those deposition heights, which corresponded to the translocated
359 amount of VLPs. Using this procedure, we quantified the VLP translocation from 3 different
360 subjects.

361 The deposition height and the translocated amount of native and PEG-crosslinked AP205
362 VLPs on tissue 3 are shown in **Figure 6**(d) and (e). A similar deposition height between
363 these VLPs was expected as tissues from the same donor were used. With tissues 1 and
364 2, the deposition heights were respectively 30 μm and 60 μm, and again remained
365 somewhat consistent between the different VLPs (**S9**). Furthermore, as shown in **Figure**
366 **6**(e), similar translocated amounts between the native and PEG-crosslinked AP205 VLPs
367 were obtained on tissue 3. This observation indicated that PEG-crosslinking did not restrict
368 nor increased VLP translocation through mucus. The translocation amount was also
369 somewhat similar between the VLPs delivered to tissues 1 and 2 (**S9**).

370 We then investigated the translocation behavior of PEGylated but not crosslinked AP205
371 VLP, namely mPEG$_{25}$-AP205 VLP^{GelRed}, on tissue 3. We found that mPEG$_{25}$-AP205
372 VLP^{GelRed} showed a similar deposition height to native and PEG-crosslinked AP205 VLPs
373 (about 40 µm, **Figure 6**(d)), however it had an increased translocation amount which
374 exceeded native AP205 VLP by two folds (**Figure 6**(e)). Particularly as compared to
375 bPEG$_{25}$-AP205 VLP, this result indicated a higher mucus permeability of the mPEG$_{25}$-
376 AP205 VLP construct. A potential explanation is an effective steric hinderance interactions
377 with mucin glycoproteins from one-end conjugated PEGs. This explanation is consistent
378 with previous reports (*64-66*).

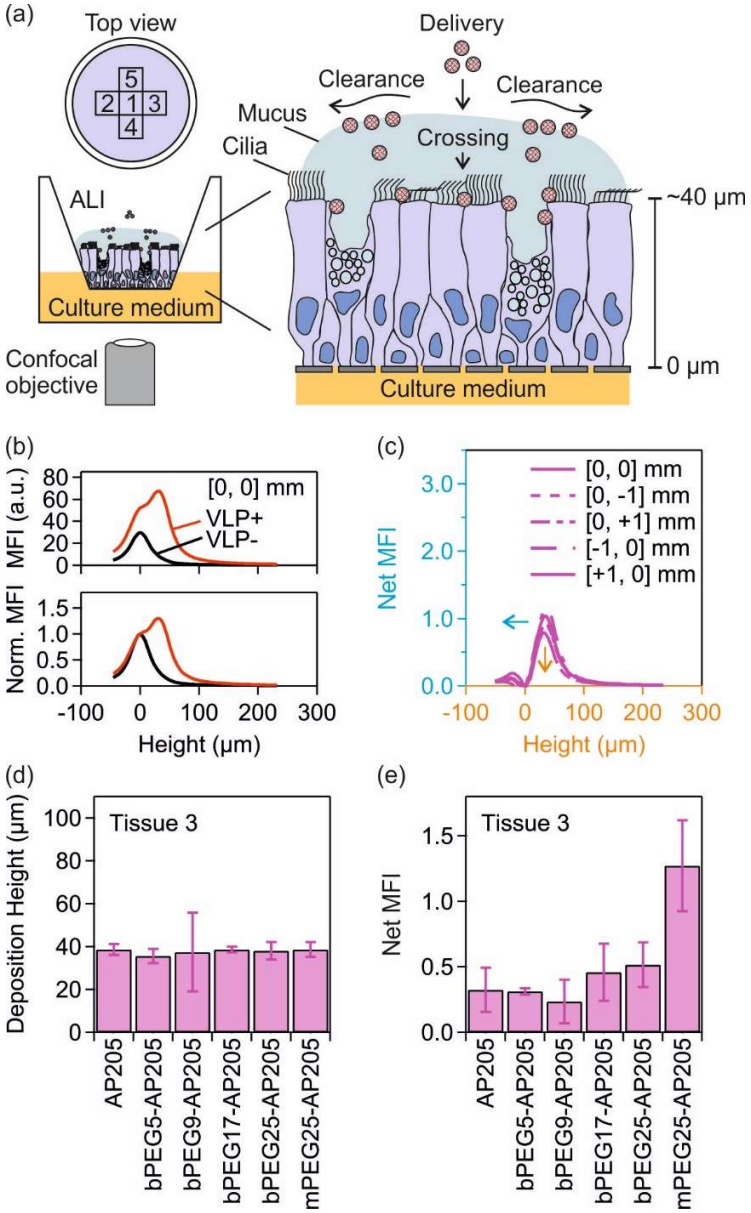

Figure 6: Translocation through mucus of AP205 VLPs in *in vitro* 3D human nasal epithelial tissues. (a) Schematic of *in vitro* nasal epithelial tissue and delivery of fluorescently-labelled virus-like particles (VLPs) from the apical side. Using laser scanning confocal microscopy (objective lens 10x, N.A. 0.3), the lateral distribution and vertical translocation through mucus of VLPs were monitored at several position 1: [0, 0] mm, 2: [-1, 0] mm, 3: [+1, 0] mm, 4: [0, -1] mm and 5: [0, +1] mm. (b) Mean fluorescence intensity (MFI) and normalized MFI (norm. MFI) variation with height collected in the center of tissue 3. MFI and norm. MFI spectra prior to VLP delivery, VLP-, and after the delivery of mPEG$_{25}$-AP205 VLP^{GelRed}, VLP+, are shown. The height of semipermeable membrane is set to 0 µm. (c) Subtracted (or net) MFI spectra on five positions showing the height location of VLP deposition and the net MFI. (d, e) The deposition height (d) and the net MFI corresponding to the translocated amount of VLPs (c) of native and PEGylated VLPs on tissue 3.

We then investigated the effect of outward-swirling mucociliary clearance on the deposition of VLPs across the tissue (*67*). In **Figure 7**, 5 µl of mPEG$_{25}$-AP205 VLP^{GelRed} solution was delivered to the center of tissue 3 in normal tissue condition or when the tissue was treated with trans-cinnamaldehyde in the basal channel. Trans-cinnamaldehyde stopped the cilia from beating throughout the measurements (*68*). Analysis of the lateral distribution of deposited VLPs across the tissue (positions 1 to 6) under normal conditions (**Figure 7**(a)) showed that a noticeable portion of VLP was cleared to the edge of the plastic insert in flowing mucus while a portion translocated similar to the observations already discussed in **Figure 6**. The lateral distribution of deposited VLPs was more uniform across the tissue when ciliary beating was stopped (**Figure 7**(b)). Additional examples of the deposited VLP distribution when ciliary beating was inhibited are shown in **SI 9**.

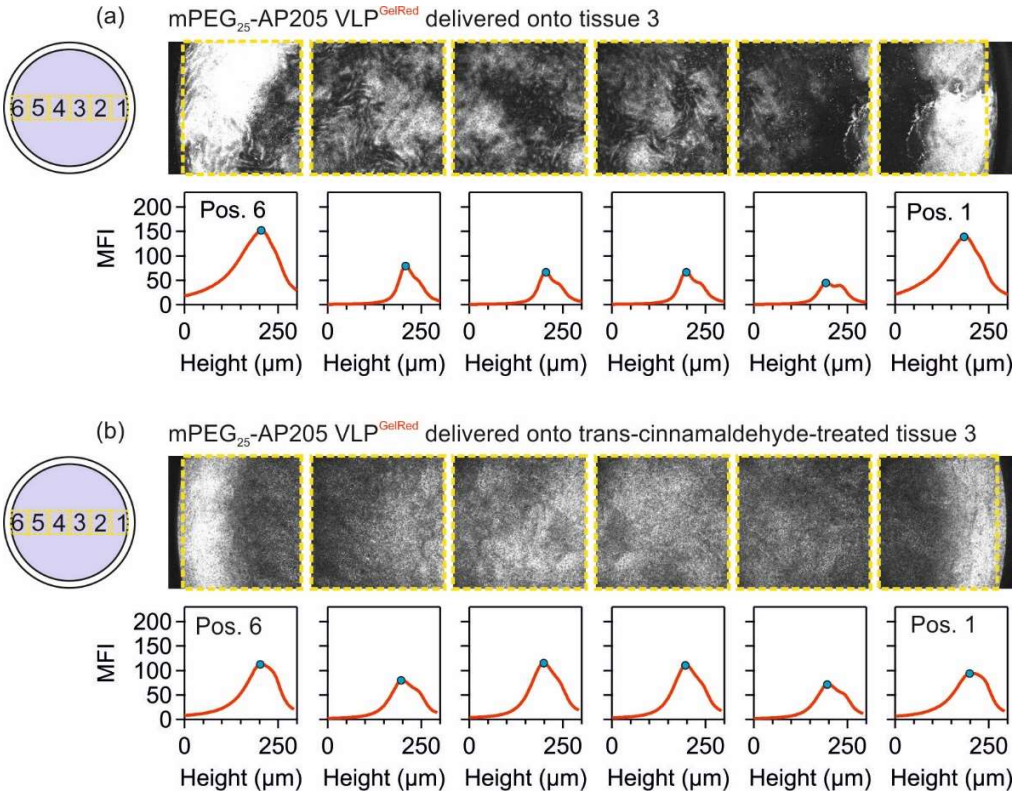

Figure 7: Effect of mucociliary clearance on translocation of VLPs across mucus. (a) Delivery of mPEG$_{25}$-AP205 VLP^{GelRed} to tissue 3. (b) Delivery of mPEG$_{25}$-AP205 VLP^{GelRed} to trans-cinnamaldehyde-treated tissue 3. The yellow box denotes the area of

411 mean fluorescence intensity (MFI) calculation and blue circle the height location of VLP
412 deposition. In these figures, height starts from above the air-liquid interface (ALI) and
413 increases in the direction of cell layer to below the semipermeable membrane. The height
414 of the semipermeable membrane is approximatively 250 µm. The individual confocal
415 images on lateral positions 1 to 6 were taken at a fixed height distance from the
416 semipermeable membrane.
417

418 **Immune activation in mouse model**

419 Recent literature points towards a growing consensus on abandoning PEG in biomedical
420 applications due to concerns associated with PEG immunogenicity. However, the lack of
421 an alternative "non-immunogenic" polymer, which bestows the beneficial properties of
422 PEG, still positions this macromolecule at high regards in pharmacy and medicine (*43, 69-*
423 *73*). For instance, PEG played an important role in mitigating SARS-Cov-2 pandemic by
424 enhancing the colloidal stability of lipid nanoparticle mRNA vaccines BNT162b2 (Pfizer
425 and BioNTech) and mRNA-1273 (Moderna). In addition, FDA guidelines of 2014
426 recommend screening for anti-PEG antibodies (*74*).

427 We investigated antibody induction against AP205 coat protein and the PEG component
428 of PEG-crosslinked AP205 VLPs in a vaccination model using C57BL/6J specific
429 pathogen free (SPF) mice. Accordingly, subcutaneous injections of VLPs without
430 additional adjuvant were performed on Day 0 and 10. The mice were sacrificed on Day 20
431 and anti-AP205 and anti-PEG serum IgG titers detected using enzyme-linked
432 immunosorbent assay (ELISA). The serum antibody titers against AP205 coat protein are
433 shown in **Figure 8**(a). As expected (*40, 41*), native AP205 VLP was immunogenic, and
434 we easily detected specific serum IgG antibodies against AP205 coat protein. Surprisingly,
435 we found that PEGylation increased the anti-AP205 IgG response titers, regardless of
436 crosslinking. Therefore, PEGylation (0.5–1.4 kDa) of AP205 VLP did not shield immune
437 activation against the coat protein; rather, specific antibody induction was increased. This
438 result could be interpreted in terms of an enhanced stability profile of AP205 VLP after
439 PEG-crosslinking. Antibody induction against the PEG coating was also investigated.
440 Consistent with the strong adjuvanticity of VLPs (*75*), the anti-PEG ELISA in **Figure 8**(b)
441 showed that the injection of PEGylated AP205 VLPs, compared to the negative control,
442 i.e., native AP205 VLP, resulted in anti-PEG IgG induction. Furthermore, the anti-PEG IgG
443 titers seemed to increase with the size of two-end conjugated PEG crosslinker, i.e., to be
444 higher in the order $bPEG_9$-AP205 VLP < $bPEG_{17}$-AP205 VLP < $bPEG_{25}$-AP205 VLP.

445

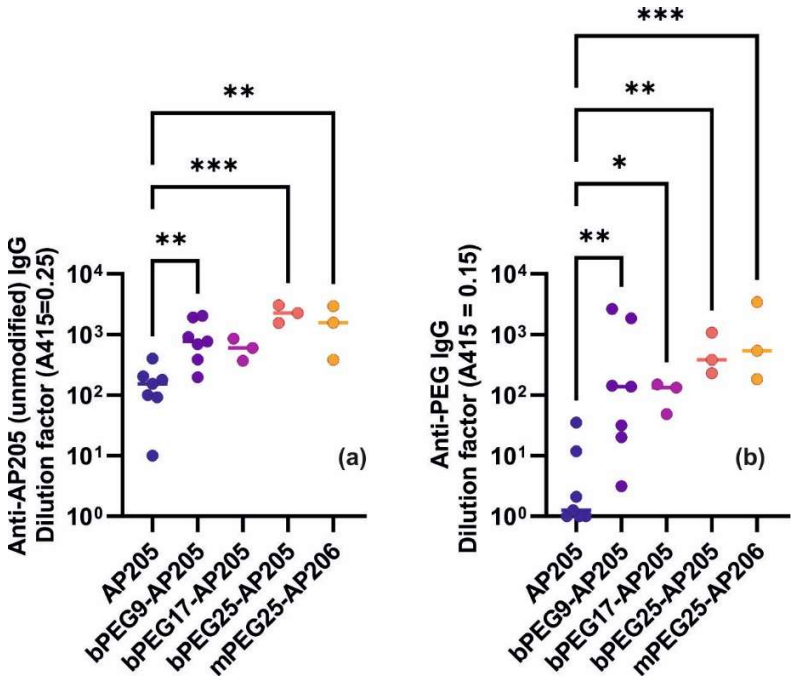

446

447 **Figure 8: Immune activation by PEG-crosslinked AP205 VLPs.** C57BL/6J SPF mice
448 were subcutaneously injected with native (n = 7), PEG-crosslinked (n = 13), or PEGylated
449 but not crosslinked (n = 3) AP205 VLPs on Day 0 and Day 10 and sacrificed on Day 20.
450 Serum antibody (IgG) titers against (a) AP205 coat protein, and (b) PEG was measured
451 by ELISA. Statistical significance was determined by ordinary one-way ANOVA with
452 Dunnett's multiple comparisons test, with a single pooled variance on log-normalized data
453 (*P = 0.0332; ***P = 0.0021; ***P = 0.0002).
454

455 # Discussion

456 VLPs have similar physical characteristics to their viruses of origin, e.g., a size in the range
457 20–200 nm, a proteinaceous core-shell structure, a patterned architecture, and target
458 specificity (*12*). Their structural properties are also similar to viruses, except for a few
459 mutations, additions, or deletions in coat protein sequence (*76, 77*). Therefore, as viruses
460 are effective only in their natural environments, it is expected that different VLPs are also
461 effective in certain, but not all, environments. In fact, all VLPs are prone to aggregation,
462 disintegration, and surface adsorption and sticking, which render them non-functional (*78*).
463 Enhancing the stability of VLPs thus seems justified in future developments of VLP
464 nanotechnology.

465 We investigated surface crosslinking of VLP capsid using PEG tethers as a means to
466 achieve the latter. PEG is characterized as a biocompatible, non-toxic, hydrophilic, and
467 stable macromolecule which upon conjugation to a particle bestows characteristics such
468 as enhanced solubility and stability, stealth from corona forming proteins and reduced
469 clearance. In fact, we found that PEG-crosslinking AP205 VLP capsid increased the
470 colloidal stability of the VLP at low pH (**S6**). In particular, while DLS showed aggregation
471 of native VLP in solution at pH 6.0, the PEG-crosslinked AP205 VLP solutions were stable
472 up to pH 4.0. Furthermore, the PEG-crosslinked VLPs were better protected against
473 proteases. Specifically, while the native AP205 VLP disintegrated somewhat quickly (less
474 than 5 min) in pig gastric fluid at pH 3.0 and 4.7, the PEG-crosslinked AP205 VLPs
475 presented a longer lifetime at the same pH values (**Figure 2** and **S7**).

476 Susceptibility of VLPs to mechanical stress is a limiting factor to their stability. Using AFM
477 force tracing, single immunoglobulin (Ig) tension sensor, and single DNA tension sensor,
478 the endocytosis "pulling" force exerted by a cell onto a virus was measured to vary in the
479 range of a few to hundreds of pN (*47-51*) and the force used by B cell to extract antigens
480 to be in the range of a few tens of pN (*52*). Using magnetic particles, an effective force
481 generated by beating cilia was also estimated to be about 62 pN (*53*). Although these *in*
482 *vivo* forces are generally below the yield force values of VLPs and virus capsids, when
483 applied repeatedly as they do *in vivo*, they can plastically deform or disintegrate the
484 capsids due to fatigue (*17-19, 23-26*). It is therefore logical to mechanically reinforce VLPs
485 in order to enhance their stability, and thereby their functionality range. PEG-crosslinking
486 increased the stiffness and strength of AP205 VLP; however, the elastic modulus
487 remained the same (**Figure 3** to **Figure 5**). Surface crosslinking of VLPs using PEG
488 tethers thus offers a viable tool to overcome the mechanical susceptibility limitation of
489 VLPs.

490 A major application of VLPs, namely delivery of antigens and drug molecules on mucosal
491 surfaces, is faced with physiological challenges, amongst which is translocation through
492 a thick mucus layer covering the epithelium. Particularly in the airways, the mucus layer
493 is subject to mucociliary clearance which further reduces VLP translocation by pushing
494 VLP laden mucus out of the airways (*62*). To mimic these challenges, we investigated the
495 translocation through mucus of native and PEG-modified AP205 VLPs in *in vitro* 3D
496 human nasal epithelial tissues with motile cilia resulting in mucociliary clearance.
497 Experiments showed an effective translocation of native AP205 VLP through mucus and

498 deposition on the epithelium against mucociliary clearance, which transported mucus in
499 swirling rotation to the edges of the tissue (*67*) (**Figure 6**). Since on these tissue mucus is
500 transported at a high speed, reaching 200 μm/s at 3 mm from the tissue center (*67*), or
501 else estimated at 40 μm/s at 1 mm from the center (*79*), a noticeable portion of AP205
502 VLP accumulated on tissue edges (**Figure 7**). Nevertheless, the results showed that the
503 diffusion of native AP205 VLP was effective against mucociliary clearance (*80-83*).

504 Although PEGylation had been shown to enhance the diffusion of synthetic nanoparticles
505 (~ 100 nm) in mucus by minimizing adhesive interactions with mucin glycoproteins (*64,*
506 *65*), the same effect had not been investigated with VLPs. An examination is required for
507 several reasons: (1) PEG coverage on VLPs is much less than the coverage on synthetic
508 nanoparticles due to scarcity of reactive sites, and (2) PEGylation may oppositely increase
509 the surface interaction forces with mucin glycoproteins by stealthing coat protein surface
510 regions that created a mild interaction, or entangling mucin glycoproteins. Therefore, we
511 examined if PEG-crosslinking may restrict the mucus penetrability of AP205 VLPs.
512 Experiments showed that similar to AP205 VLP one portion of VLPs translocated through
513 mucus while the other portion cleared to the edges via mucociliary clearance. Therefore,
514 PEG-crosslinking did not inhibit the VLPs diffusion in mucus. Additional experiments
515 showed that the translocated portion increased when the VLP was PEGylated but not
516 crosslinked, as well as when mucociliary clearance was inhibited. Altogether, PEGylation
517 is found to be effective in bestowing mucus penetrability to VLPs and may enhance the
518 latter when the coverage is increased, for example with CPMV and AdV which have a
519 higher number of surface reactive sites compared to AP205 VLP.

520 These discussions raise the question, is mucus a poor barrier to VLPs, particularly those
521 of the size range below about 100 nm, including AP205 VLP (27.6 nm, this work), and
522 VLPs of human papilloma virus and Norwalk virus (respectively, 55 nm and 38 nm, (*80*))?
523 Considering viruses that infect mucosal surfaces, including polio (28 nm), hepatitis B (43
524 nm), adenoviruses (60–90 nm), rotavirus (75 nm), human immunodeficiency virus (120
525 nm) and herpes simplex virus (180 nm) (*83*), one may conclude that viruses of small
526 enough size are capable of deeply penetrating the mucus. This is expected when the pore
527 size of mucus gel (100–5000 nm) exceeds the size of these viruses. Penetration is
528 additionally facilitated by the patchy surface charge distribution on virus surface (*80, 83*).
529 As already discussed, surface conjugation with polymers introduces new interactions
530 (e.g., electrostatic, and hydrophobic) with mucus which may affect the fate of the modified

VLPs in mucosal applications. For example, a single mutation in adeno-associated virus (AAV) serotype 6 was found to increase the diffusion rate in mucus compared to AAV1. We found that surface conjugation of PEG with MW 0.5–1.4 kDa did not change VLP size and did not interfere with the penetration behavior of the VLPs in mucus (**Figure 5** and **Figure 6**).

Finally, our results show that the colloidal properties of VLPs are relevant variables that should be further investigated in mucosal applications. As schematically shown in **Figure 9**, after mucosal delivery, the population of VLPs reaching the epithelial cell layer increases when the rates of protease destabilization, pH-induced aggregation, and mechanical disintegration are reduced, and when the diffusion rate in flowing mucus is increased. PEG-crosslinking of multiple surface sites is therefore a promising approach to improve and extend the range of VLP mucosal functions. PEG immunogenicity is certainly a limiting factor. However, since VLPs are inherently immunogenic, the overall enhanced functionality, strength and stability may overcome the PEG-immunogenicity concern.

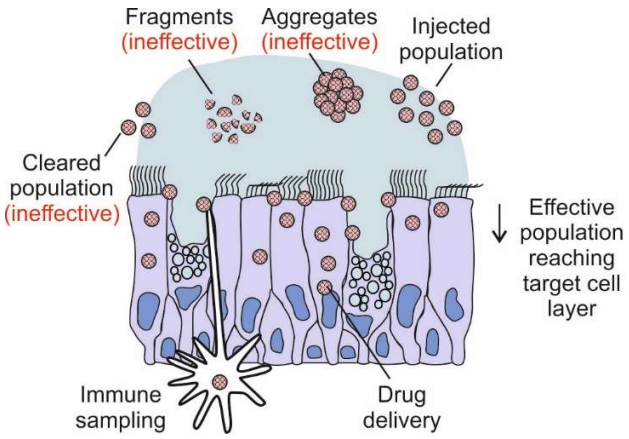

Figure 9: Fate of delivered VLPs in mucosal applications. Effective VLPs, i.e., those reaching the underlying epithelium, remain stable against stresses that lead to aggregation (e.g., by pH), destabilization (e.g., by proteases), and disintegration (e.g., by mechanical stress) and show high mucus penetrability (against e.g., mucociliary clearance).

Materials and Methods

Experimental Design

555 Surface crosslinking of virus-like particle (VLP) capsids using polyethylene glycol (PEG)
556 tethers was investigated against physiological challenges to assess its performance on
557 mucosal surfaces. The model native VLP was derived from the coat protein of
558 Acinetobacter phage, namely AP205 VLP. PEG tethers included two-end functional PEG
559 molecules of various molecular weights. The PEG-crosslinked AP205 VLPs were initially
560 evaluated in terms of the reaction products and the sites of PEG conjugation to reactive
561 surface sites (using a combination of dynamic light scattering, transmission electron
562 microscopy, reducing SDS-polyacrylamide gel electrophoresis, electrospray ionization
563 mass spectroscopy and nano ultra-performance liquid chromatography-MS) and then
564 investigated for the aggregation behavior against pH (using dynamic light scattering),
565 disintegration against digestive enzymes from pig and mouse gastric fluid (using agarose
566 gel electrophoresis), resistance to mechanical force (using atomic force microscopy), and
567 penetration in mucus in the presence of motile cilia and mucociliary clearance (using *in*
568 *vitro* 3D human nasal tissues).
569

570 **Production of AP205 VLP**

571 The biosynthesis of AP205 VLP is reported in details in our previous study (*26*). Briefly, it
572 includes the expression of recombinant AP205 coat proteins in bacterial cytoplasm which
573 then self-assemble into AP205 VLPs. After the expression of VLP, a series of steps
574 consisting of bacterial lysis, digestion of RNA and DNA contaminants, and extraction of
575 lipids were performed prior to precipitation and dialysis against PBS to produce purified
576 AP205 VLPs. Plasmids were generated by custom DNA synthesis (Twist Bioscience, San
577 Francisco, CA, USA) of the expression cassettes and cloning into the pRSFDuet-1
578 (Novagen) backbone between the PfoI and BshTI restriction sites. Sequences of the
579 plasmids are available via the ETH-Zürich research collection at
580 https://doi.org/10.3929/ethz-b-000556182. The sequence of AP205 monomer and the
581 description of plasmid are reported in **S1**.

582 **PEGylation of AP205 VLP**

583 The functional group on the extremities of homobifunctional PEG crosslinker molecules
584 (bPEG_n, n = 5 to 25) and on one extremity of monofunctional PEG molecules (mPEG_n, n
585 = 12 and 25) was NHS-ester which is reactive to primary amine of lysine residues and N-
586 terminus of AP205 coat proteins. Reactions with native AP205 VLP proceeded at 1–100x
587 molar ratio of crosslinker molecule to AP205 monomer (

588 molar ratio = [functional moleucle]/[AP205 CP]). The PEG molecule was dissolved in
589 anhydrous and molecular sieves dried dimethyl sulfoxide (DMSO, Sigma-Aldrich) to a
590 concentration of 100 mM. An appropriate amount was then added to AP205 VLP
591 suspension at 4 mg/ml in PBS. The reaction was left for 24 h at 4°C. Then after, it was
592 quenched by adding Tris•HCl (Trizma® base, Sigma-Aldrich, and hydrochloric acid 37%,
593 VWR) at 20–50 mM and incubating for 15 min. Unreacted PEG molecules and Tris were
594 removed using Zeba Spin Desalting Column (ThermoFisher) with molecular weight cut-off
595 at 7 kDa. Other reactive molecules including BS^3 and Sulfo-NHS were used similarly;
596 however, they were initially dissolved to 100 mM in PBS. A summary of the physical
597 properties of these molecules is provided in **S1**.

598 **Fluorescent staining of VLPs**

599 We defined a mixing ratio $x = \text{mass of stain}/\text{mass of VLP} = 10^{-2}$, and a final stained VLP
600 concentration equal to 5.3 mg/ml. (To calculate the mass of stain, we assumed 10,000x
601 to correspond to 10 mg/ml.) GelRed® (10,000x in water, biotium) or SYBRGold™ (10,000x
602 in DMSO) were used and staining proceeded for 30 min. To remove unbound dye, the
603 solution of stained VLP was buffer exchanged with pure PBS using Zeba™ Spin Desalting
604 Columns (7,000 MWCO, ThermoFisher). We note that since the columns contained
605 sodium azide, it was important to buffer the column with pure PBS prior to cleaning the
606 stained VLP solution. The stained VLP solution was finally filtered using 0.2 µm centrifuge
607 filters (Corning® Costar® Spin-X® centrifuge tube filters) to remove possible aggregates.
608 The intensity of stained VLPs was monitored over time using laser scanning confocal
609 microscopy and showed no noticeable reduction over a course of at least two weeks.

610 **Transmission electron microscopy (TEM)**

611 4 µl VLP solution (0.1 mg/ml) was deposited on glow-discharged (45 sec, 25 mA, negative
612 charge) carbon-coated grids (Ted Pella) for 1-5 min, after which the excess liquid was
613 removed using filter paper. Then the grid was rinsed with 5 µl of PBS to remove loosely
614 bound VLPs. Subsequently, 3 µl of 2% uranyl acetate was applied and immediately
615 removed with filter paper prior to a second treatment with 3 µl of 2% uranyl acetate for 20
616 sec. Excess liquid was again collected using filter paper and the grid was let dry at room
617 temperature (RT). Data acquisition was performed using a Morgani transmission electron
618 microscope operating at 100 kV acceleration voltage.

619 **Electrospray ionization mass spectrometry (ESI-MS)**

620 ESI-MS was acquired on a Synapt G2-Si quadrupole time-of-flight spectrometer (Waters,
621 UK) with a capillary voltage of 3 V, a cone voltage of 50 V and a source temperature of
622 100°C. VLPs at a concentration of 1 mg/ml were reduced by dithiothreitol (DTT) at a final
623 concentration of 50 mM. The reduction was performed for 1 h at RT and at pH 8. The
624 samples were acidified with 1% formic acid (Thermo, USA), desalted using C4 Zip Tips
625 (Millipore, USA) and analyzed in methanol:2-propanol:0.2 % formic acid (30:20:50). The
626 solutions were infused through a fused silica capillary (ID 75 µm) at a flow rate of 1 µl/min
627 and sprayed through Pico Tips (ID 30 µm). The last were obtained from New Objective
628 (Woburn, MA, USA). Recorded m/z data were deconvoluted using the MaxEnt1 software
629 (Waters, UK) with a resolution of the output mass of 0.5 Da per channel and a Uniform
630 Gaussian Damage Model at the half-height of 0.5 Da.

631 **Nano ultra-performance liquid chromatography-MS (nanoUPLC-MS/MS)**

632 NanoUPLC-MS/MS was acquired on Thermo FUSION mass spectrometer (Thermo,
633 Germany) coupled to a nano-M-class UPLC system (Waters). $BPEG_9$-AP205 VLP at a
634 concentration of 1 mg/ml was digested by incubating 3 µl of the sample with 42 µl of 25
635 mM ammonium bicarbonate (pH 8.5) and 1 µl of TCEP (100 mM) for 1 h at 37°C. Reduced
636 protein was incubated with 2 µl chloroacetamide (500 mM) for 1 h at 37°C. Then after, 5
637 µl trypsin (0.1 µg/µl in 10 mM HCl) was added and the solution further incubated overnight
638 at 37°C. When needed the pH was adjusted to pH 8. At the end of this procedure, the
639 sample was dried using SpeedVac. Digested and dried sample was dissolved in 20 µl
640 ddH_2O with 0.1% formic acid and diluted 5 times before transferring to autosampler vials.
641 Peptides were resuspended in 2.5% acetonitrile with 0.1% formic acid and loaded onto a
642 nanoEase M/Z Symmetry C18 (75 µm × 20 mm, 100 Å, 3 µm particle size) and separated
643 on a nanoEase M/Z HSS C18 T3 (75 µm × 150 mm, 130 Å, 1.7 µm particle size) at a
644 constant flow rate of 300 nl/min, with a column temperature of 50°C and a linear gradient
645 of 2−32% acetonitrile/0.1% formic acid in 79 min, and then 32-45% acetonitrile/0.1%
646 formic acid in 10 min, followed by a sharp increase to 98% acetonitrile in 2 min and then
647 held isocratically for another 10 min. Mass spectrometer was operated under data-
648 dependent acquisition (DDA), one scan cycle comprised of a full scan MS survey
649 spectrum, followed by up to 12 sequential HCD MS/MS on the most intense signals above
650 a threshold of 1e4. Full-scan MS spectra (600–2000 m/z) were acquired in the FT-Orbitrap
651 at a resolution of 70,000 at 400 m/z, while HCD MS/MS spectra were recorded in the FT-
652 Orbitrap at a resolution of 35,000 at 400 m/z. HCD was performed with a target value of

653 1e5 and normalization collision energy 25 (units?) was applied. AGC target values were
654 5e5 for full FTMS. For all experiments, dynamic exclusion was used with a single repeat
655 count, 15 s repeat duration, and 30 s exclusion duration. The acquired MS data were
656 processed for identification using the Byonic search engine (PMI). The spectra were
657 searched against AP205 VLP sequence and AP205 VLP sequence with E. *Coli* database.
658 The following modifications were included: (a) variable modifications, namely oxidation at
659 N-terminus methionine and carbamidomethylation (C), and (b) user-defined modifications,
660 namely 478.2565 ($C_{22}O_{11}H_{38}$) was set for PEG_9-crosslinked peptides and 496.2565
661 ($C_{22}O_{12}H_{40}$) for one-end PEG_9 conjugation at a lysine residue or N-Terminus. In this
662 analysis, the raw data were analysed by two software, PMI Byonic search engine and SIM
663 1.5.5.3 (Spectrum identification machine) (*84*). In addition, two fasta database with and
664 without starting methionine was used to confirm the N-terminus.

665 **SDS-polyacrylamide gel electrophoresis (SDS-PAGE)**

666 Denaturing and reducing SDS-PAGE was carried out in 13% Tricine gels. Samples of 3
667 µg of VLP were denatured and reduced in Laemmli sample buffer at 95°C for 5 min prior
668 to electrophoresis. Proteins were visualized by Coomassie staining.

669 **Dynamic light scattering (DLS)**

670 DLS was performed at a fixed angle of 173° by averaging 3 runs of 30-s long each using
671 Zetasizer Nano (Malvern Panalytical). The time correlation function of scattered intensity
672 was analyzed by the cumulant as well as CONTIN methods. The VLP concentration was
673 initially adjusted to 0.1 mg/ml in filtered PBS prior to measurements.

674 **Gastric fluid collection**

675 Pig gastric content was collected from the stomach of conventionally reared, outbred pigs
676 with different genetic contributions of French-Swiss Landrace and Swiss Large White.
677 Total gastric content was collected. Mouse gastric content was obtained by collecting total
678 stomach content from several specific opportunistic pathogen-free (SPF) C57BL/6J WT
679 mice. The gastric content from several mice was pooled to have sufficient volume. Pig or
680 mouse gastric content was centrifuged for 5 min at 16000 rpm to separate the non-
681 digested food particles. After the collection of supernatant (gastric fluid), it was filtered
682 using 0.22 µm sterile filter and the pH measured using a laboratory pH-meter.

683 **Agarose gel electrophoresis**

684 VLPs from 1 mg/ml preparation were diluted 1:10 in pig or mouse gastric fluid and
685 incubated for 5 min, 30 min, 1 h and 1.5 or 2 h at 37°C. After each incubation, the samples
686 were immediately placed on ice. Native agarose gel electrophoresis of PBS- or gastric
687 fluid-treated VLPs was carried out in 0.6% agarose in TAE buffer (40 mM Tris, 0.1% acetic
688 acid, 1 mM EDTA) with 0.5 µg/ml of ethidium bromide for visualization. Samples of 5 µg
689 VLP were electrophoresed at 120 Volts for 1 h, then imaged on a UV transilluminator.

690 **Atomic force microscopy (AFM)**

691 The schematic of AFM measurements is shown in **Figure 3**(a). After an initial calibration,
692 which included also the calibration of PeakForce tapping mode, on freshly cleaved mica,
693 the tip was brought in proximity to VLPs immobilized at a concentration of 5 µg/ml on
694 Highly Oriented Pyrolytic Graphite (HOPG, Ted Pella, Inc.) The calibrated parameters
695 included stiffness (59.4–82.0 pN/nm) using thermal method and optical lever sensitivity
696 using cantilever–mica contact region (*85*), and drive3 amplitude sensitivity. During the
697 transport of cantilever from mica to HOPG, the cantilever remained wet, and the laser spot
698 was checked to remain on the same spot. The calibration values were re-measured on
699 mica at the end of the measurements to detect any noticeable variation to the calibrated
700 parameters. Single VLPs were localized on HOPG by imaging in PeakForce tapping mode
701 (peak force 50 pN, tapping frequency 1 kHz, amplitude 30 nm). Generally, images of
702 individual VLPs were acquired at a scan rate of 0.7 Hz with 200×200 or 500×500 nm^2 scan
703 size and a resolution of 64 points per line, leading to a pixel size of 3 nm. After localization,
704 we used “Point & Shoot” function (NanoScope, Bruker) to place the AFM tip on the apex
705 of selected VLPs before applying indentation using Ramp mode. The VLPs were indented
706 up to a threshold force value of 400 pN at a preset frequency of 1 Hz, which resulted in an
707 indentation force rate of about (4–9)×10^3 pN/s. Indented particles were imaged again in
708 PeakForce tapping to detect signs of degradation, drift, or displacement due to tip lateral
709 forces. The height of individual VLPs before (H_i) and after (H_f) indentation were
710 calculated by placing a trace line over the particles on images previously flattened using
711 Gwyddion 2.47 (*86*). For stiffness evaluation, we proceeded as follows: deflection versus
712 piezo displacement was converted to force versus tip separation using protocols written
713 in Igor Pro (Wavemetrics). Fit to force versus indentation distance ($F-\delta$) curve in the
714 linear response part of the tip–VLP contact region gave the stiffness ($k = dF/d\delta$) and the
715 indentation ($\delta = \Delta F/k$). The fit was performed in the force range $50\,\mathrm{pN} \le F \le 250\,\mathrm{pN}$, and

716 only those VLPs with indentation range $2.0 \leq \delta \leq 6.0\,\mathrm{nm}$ were selected for averaging. Only
717 one indentation per VLP was used for the evaluations. The indentation force rate ($\dot{F}$) was
718 calculated from a linear fit to the force versus indentation time ($F-t$) curve in the same
719 region were the stiffness of VLP was calculated. Strain rate was then calculated from the
720 relation $\dot{\gamma} = \dot{F}/k\delta$. Average stiffness was calculated from at least duplicate independent
721 VLP preparations. UV-ozone (Novascan) cleaned AC40 BioLever Mini cantilevers
722 (Bruker) were used. Dimension FastScan (Bruker) was used for imaging and force
723 spectroscopy.

724 **Small angle X-ray scattering (SAXS)**

725 We used a Xeuss 2.0 (Xenocs, France) instrument with a microfocused X-ray source at
726 the Laboratory Léon Brillouin (LLB NIMBE CEA Saclay). The Cu Kα radiation ($\lambda_{Cu\ K\alpha}$ =
727 1.5418 Å), and the data were collected by a 2D Pilatus 1 M detector (Dectris, Switzerland).
728 The scattering vector $q = 4\pi/\lambda \sin(\theta/2)$, with θ being the scattering angle was calibrated
729 using silver behenate. Data were collected and azimuthally averaged to produce
730 unidimensional intensity versus q, with q interval of 0.005 to 0.1 $Å^{-1}$. The measurements
731 were performed at 25°C. The scattering intensity was collected for 2600 s. The intensity
732 was corrected for sample thickness, transmission, and acquisition time. The modelling of
733 the integrated data was performed with a core-shell form factor, and a hard sphere
734 structure factor, when needed, using the SasView software.

735 ***In vitro* 3D human nasal epithelial tissue**

736 *In vitro* human nasal epithelial tissues from single donors (MucilAir™) were obtained from
737 Epithelix (Switzerland). The tissues were maintained according to company's protocols
738 and included tissue 1 from a Caucasian 64-year-old female subject (MD0860), tissue 2
739 from a Caucasian 46-year-old male subject (MD0871) and tissue 3 from a Caucasian 38-
740 year-old male subject (MD0774). The subjects were non-smokers and had no history of
741 respiratory pathology.

742 **Inhibition of mucociliary clearance**

743 Ciliary beating was inhibited using trans-cinnamaldehyde (97%, C80687, Sigma-Aldrich).
744 Trans-cinnamaldehyde was dissolved in MucilAir™ culture medium to a concentration of
745 30 mM. To improve solubility, freshly prepared solution was sonicated for 15 min and the
746 solution was kept at 37°C prior to filling the basal channel of MucilAir™ monodonor nasal

747 epithelial tissue. After 20 min of incubation, the ciliary beating stopped, and no recovery
748 was observed for up to 2 h.

749 **Delivery of VLPs to *in vitro* 3D human nasal epithelial tissue**

750 Tissues were incubated in a humidified-CO_2 chamber at 37°C. After a period of
751 equilibration 0.5–1 h, 5 µl of VLP solution (5.3 mg/ml) was delivered from the apical side.
752 The delivery was onto the center of the tissue.

753 **Laser scanning confocal microscopy (LSCM)**

754 Lateral distribution and vertical translocation of fluorescently labelled VLPs through mucus
755 were then monitored using laser scanning confocal microscopy (LSCM, Leica SP5
756 confocal microscope). We used a 10x objective lens with N.A. 0.3. Excitation wavelength
757 $\lambda_{ex} = 488\ \mathrm{nm}$ was used for SYBRGold™- stained VLPs and Salmonella vaccine with
758 detection wavelength $\lambda_{em} = 500 - 590\ \mathrm{nm}$. $\lambda_{ex} = 514\ \mathrm{nm}$ was used for GelRed®-stained
759 VLPs with $\lambda_{em} = 550 - 650\ \mathrm{nm}$. The channel spectral detection was set to HyD (Gain equal
760 to 100). The mean fluorescence intensity (MFI) variation with height was collected in the
761 center [0, 0] mm, and on positions [-1, 0] mm, [+1, 0] mm, [0, -1] mm and [0, +1] mm prior
762 to, during and after VLP delivery. Leica LAS AF software was used for saving the images.
763 Analysis was performed using ImageJ.

764 **Mice**

765 All animal experiments were performed in accordance with Swiss Federal regulations
766 approved by the Commission for Animal Experimentation of the Kanton Zurich (license
767 ZH009/2021, Kantonales Veterinäramt Zürich, Switzerland). SPF C57BL/6J WT mice
768 were used in all experiments. Mice were bred and housed in individually ventilated cages
769 with a 12 h light/dark cycle in the ETH Phenomics Center (EPIC, RCHCI), ETH Zürich,
770 and were fed a standard chow diet. All mice included in experiments were 7 weeks or
771 older and objectively healthy as determined by routine health checks. Wherever possible
772 an equal number of males and females was used in each experimental group.

773 **Subcutaneous injection**

774 50 µg of VLP in 100 µl of PBS was subcutaneously injected into the loose skin over the
775 interscapular area of C57BL/6J SPF mice on Day 0 and Day 10. The mice were
776 euthanized on Day 20. Blood was collected by cardiac puncture, and serum separated by

777 spinning 1.1 ml serum gel tubes (Sarstedt) at 10,000 g for 5 min at 20°C in a conventional
778 table-top centrifuge, and heat-inactivated for 30 min at 56°C.

779 **Enzyme-linked immunosorbent assay (ELISA) for detection of anti-AP205 IgG**
780 **response**

781 50 µl of AP205 VLP solution (5 µg/ml) was pipetted into an appropriate number of wells of
782 ELISA plates (4 Nunc MaxiSorp flat bottom 96-well plates) and the VLP allowed to adsorb
783 overnight at 4°C. The wells were washed three times with wash buffer (0.05% Tween 20
784 in PBS) and blotted. The wells were blocked using 150 µl of blocking buffer (2% bovine
785 serum albumin in PBS) for 1.5 h at RT. Subsequently, the wells were washed five times
786 with wash buffer and blotted. Mouse sera were diluted ten times in blocking buffer, and
787 sequentially in 1:3 dilution steps added to the wells of ELISA plates. The plates were
788 incubated for 2 h at RT to allow the binding of serum IgG to AP205 proteins. Goat anti-
789 mouse IgG-HRP (Sigma) was diluted a thousand-fold in blocking buffer, and 50 µl of
790 solution added to the wells and incubated for 1 h at RT. The wells were washed five times
791 using wash buffer and blotted. Finally, 150 µl of freshly prepared substrate solution
792 (consisting of 0.1 M NaH_2PO_4 (substrate buffer), 2,2'-azino-bis(3-ethylbenzothiazoline-6-
793 sulfonic acid (1–2 mg per 10 ml of substrate buffer), and H_2O_2 (10 µl per 10 ml)) was added
794 to each well. The plate was incubated in the dark for 40 min. On Tecan (Tecan Infinite 200
795 PRO microplate reader), absorbance was measured at 415 nm. The reference wavelength
796 for the subtraction of background signal was set to 480 nm.

797 **Enzyme-linked immunosorbent assay (ELISA) for detection of anti-PEG IgG**
798 **response**

799 Mouse sera were diluted ten times in PEG dilution buffer (PEGD50-1, Life Diagnostics,
800 Inc.), and sequentially in 1:3 dilution steps added to the wells of PEG-BSA coated ELISA
801 plates (PBSA20PL, Life Diagnostics, Inc.) The plates were incubated for 2 h at RT to allow
802 antibody binding. The wells were washed five times with 300 µl PEG wash buffer
803 (PEGW50-20, Life Diagnostics, Inc.) and blotted. Goat anti-mouse IgG-HRP (AP124P,
804 Sigma-Aldrich) was diluted a thousand-fold in PEG dilution buffer and 100 µl of this
805 solution was added to each well with an incubation of 1 h at RT. The wells were washed
806 and blotted again. Finally, 150 µl of freshly prepared substrate solution was added to each
807 well. The plates were incubated in the dark for 40 min. On Tecan (Tecan Infinite 200 PRO

808 microplate reader), absorbance was measured at 415 nm. The reference wavelength for
809 the subtraction of background signal was set to 480 nm.

810 **Statistical Analysis**

811 AFM and LSCM results were expressed as mean ± standard deviation analyzed by Igor
812 Pro from WaveMetrics. *In vivo* mouse vaccination results were assessed using ordinary
813 one-way ANOVA with Dunnett's multiple comparisons test using GraphPad Prism
814 (*P = 0.0332; ***P = 0.0021; ***P = 0.0002).
815

816

Acknowledgments

We acknowledge the contributions from Till Germerdonk in DLS measurements, and discussions with Patrick Zueblin. We also acknowledge the time for SAXS measurements provided by the Leon Brillouin Laboratory (LLB), and the support of Fabrice Cousin.

Funding

European Research Council (ERC) Grant number 865730 (MR, YT, AA and ES)

Swiss National Science Foundation, Switzerland, rant number IZSEZ0_212991 (MR)

Swiss National Science Foundation, Switzerland, grant numbers 40B2-0_180953 (ES)

Swiss National Science Foundation, Switzerland, grant numbers 310030_185128 (ES)

National Center for Competence in Research in Microbiomes, Switzerland (ES)

Botnar Research Centre for Child Health Multi-investigator project “Microbiota Engineering for Child Health” (ES)

Gebert Rüf Microbials, grant number GR073_17 (ES)

Cystic Fibrosis Trust UK SRC 016 (PC, JK, RF)

EU ITN PhyMot (EC)

Author contributions

Conceptualization: MR

Methodology: MR, PC, RM, ES

Investigation: MR, AA, SG, VL, TK, YT, WLB, EC, SC, CWL, JK

Writing—original draft: MR

Writing—review & editing: All authors

Funding acquisition: MR, PC, ES

Competing interests

Authors declare that they have no competing interests.

Data and materials availability

All data used in the analyses are available without limitation from the first author.

Supplementary Materials

Further information regarding the Materials and Methods are provided in Supplementary Materials (**S**).

References

1. Y. H. Chung, H. Cai, N. F. Steinmetz, Viral nanoparticles for drug delivery, imaging, immunotherapy, and theranostic applications. *Advanced Drug Delivery Reviews* **156**, 214-235 (2020).
2. H. Tariq, S. Batool, S. Asif, M. Ali, B. H. Abbasi, Virus-Like Particles: Revolutionary Platforms for Developing Vaccines Against Emerging Infectious Diseases. *Frontiers in Microbiology* **12**, (2022).
3. H. Hu, N. F. Steinmetz, Development of a Virus-Like Particle-Based Anti-HER2 Breast Cancer Vaccine. *Cancers* **13**, (2021).
4. D. Yin, S. Ling, D. Wang, Y. Dai, H. Jiang, X. Zhou, S. R. Paludan, J. Hong, Y. Cai, Targeting herpes simplex virus with CRISPR-Cas9 cures herpetic stromal keratitis in mice. *Nat Biotechnol* **39**, 567-577 (2021).
5. S. Banskota, A. Raguram, S. Suh, S. W. Du, J. R. Davis, E. H. Choi, X. Wang, S. C. Nielsen, G. A. Newby, P. B. Randolph, M. J. Osborn, K. Musunuru, K. Palczewski, D. R. Liu, Engineered virus-like particles for efficient in vivo delivery of therapeutic proteins. *Cell* **185**, 250-265.e216 (2022).
6. J. Mianné, A. Nasri, C. N. Van, C. Bourguignon, M. Fieldès, E. Ahmed, C. Duthoit, N. Martin, H. Parrinello, A. Louis, A. Iché, R. Gayon, F. Samain, L. Lamouroux, P. Bouillé, A. Bourdin, S. Assou, J. De Vos, CRISPR/Cas9-mediated gene knockout and interallelic gene conversion in human induced pluripotent stem cells using non-integrative bacteriophage-chimeric retrovirus-like particles. *BMC Biology* **20**, 8 (2022).
7. C. Sakai, K. Hosokawa, T. Watanabe, Y. Suzuki, T. Nakano, K. Ueda, M. Fujimuro, Human hepatitis B virus-derived virus-like particle as a drug and DNA delivery carrier. *Biochemical and Biophysical Research Communications* **581**, 103-109 (2021).
8. E. C. Thuenemann, D. H. T. Le, G. P. Lomonossoff, N. F. Steinmetz, Bluetongue Virus Particles as Nanoreactors for Enzyme Delivery and Cancer Therapy. *Mol Pharm* **18**, 1150-1156 (2021).
9. S. Panthi, P. T. Schmitt, F. J. Lorenz, B. A. Stanfield, A. P. Schmitt, Paramyxovirus-Like Particles as Protein Delivery Vehicles. *J Virol* **95**, e0103021 (2021).
10. A. Shahrivarkevishahi, M. A. Luzuriaga, F. C. Herbert, A. C. Tumac, O. R. Brohlin, Y. H. Wijesundara, A. V. Adlooru, C. Benjamin, H. Lee, P. Parsamian, J. Gadhvi, N. J. De Nisco, J. J. Gassensmith, PhotothermalPhage: A Virus-Based Photothermal Therapeutic Agent. *J Am Chem Soc* **143**, 16428-16438 (2021).
11. H. Lee, A. Shahrivarkevishahi, J. L. Lumata, M. A. Luzuriaga, L. M. Hagge, C. E. Benjamin, O. R. Brohlin, C. R. Parish, H. R. Firouzi, S. O. Nielsen, L. L. Lumata, J. J. Gassensmith, Supramolecular and biomacromolecular enhancement of metal-free magnetic resonance imaging contrast agents. *Chemical Science* **11**, 2045-2050 (2020).
12. A. Armanious, M. Radiom, R. Mezzenga, Recent Experimental Advances in Probing the Colloidal Properties of Viruses. *Current Opinion in Colloid & Interface Science*, 101703 (2023).
13. M. F. Bachmann, G. T. Jennings, Vaccine delivery: a matter of size, geometry, kinetics and molecular patterns. *Nature Reviews Immunology* **10**, 787-796 (2010).
14. V. Sankar, V. Hearnden, K. Hull, D. V. Juras, M. Greenberg, A. Kerr, P. Lockhart, L. Patton, S. Porter, M. Thornhill, Local drug delivery for oral mucosal diseases: challenges and opportunities. *Oral Diseases* **17**, 73-84 (2011).
15. J. O. Morales, K. R. Fathe, A. Brunaugh, S. Ferrati, S. Li, M. Montenegro-Nicolini, Z. Mousavikhamene, J. T. McConville, M. R. Prausnitz, H. D. C. Smyth, Challenges and Future Prospects for the Delivery of Biologics: Oral Mucosal, Pulmonary, and Transdermal Routes. *The AAPS Journal* **19**, 652-668 (2017).
16. S. Hua, Advances in Oral Drug Delivery for Regional Targeting in the Gastrointestinal Tract - Influence of Physiological, Pathophysiological and Pharmaceutical Factors. *Frontiers in Pharmacology* **11**, (2020).

17. I. L. Ivanovska, P. J. d. Pablo, B. Ibarra, G. Sgalari, F. C. MacKintosh, J. L. Carrascosa, C. F. Schmidt, G. J. L. Wuite, Bacteriophage capsids: Tough nanoshells with complex elastic properties. *Proceedings of the National Academy of Sciences* **101**, 7600-7605 (2004).
18. J. P. Michel, I. L. Ivanovska, M. M. Gibbons, W. S. Klug, C. M. Knobler, G. J. L. Wuite, C. F. Schmidt, Nanoindentation studies of full and empty viral capsids and the effects of capsid protein mutations on elasticity and strength. *Proceedings of the National Academy of Sciences* **103**, 6184-6189 (2006).
19. N. Kol, M. Gladnikoff, D. Barlam, R. Z. Shneck, A. Rein, I. Rousso, Mechanical Properties of Murine Leukemia Virus Particles: Effect of Maturation. *Biophysical Journal* **91**, 767-774 (2006).
20. C. Carrasco, A. Carreira, I. A. T. Schaap, P. A. Serena, J. Gómez-Herrero, M. G. Mateu, P. J. d. Pablo, DNA-mediated anisotropic mechanical reinforcement of a virus. *Proceedings of the National Academy of Sciences* **103**, 13706-13711 (2006).
21. N. Kol, Y. Shi, M. Tsvitov, D. Barlam, R. Z. Shneck, M. S. Kay, I. Rousso, A Stiffness Switch in Human Immunodeficiency Virus. *Biophysical Journal* **92**, 1777-1783 (2007).
22. I. Ivanovska, G. Wuite, B. Jönsson, A. Evilevitch, Internal DNA pressure modifies stability of WT phage. *Proceedings of the National Academy of Sciences* **104**, 9603-9608 (2007).
23. A. Llauró, D. Luque, E. Edwards, B. L. Trus, J. Avera, D. Reguera, T. Douglas, P. J. d. Pablo, J. R. Castón, Cargo–shell and cargo–cargo couplings govern the mechanics of artificially loaded virus-derived cages. *Nanoscale* **8**, 9328-9336 (2016).
24. A. Ortega-Esteban, G. N. Condezo, A. J. Pérez-Berná, M. Chillón, S. J. Flint, D. Reguera, C. San Martín, P. J. de Pablo, Mechanics of Viral Chromatin Reveals the Pressurization of Human Adenovirus. *ACS Nano* **9**, 10826-10833 (2015).
25. M. Jiménez-Zaragoza, M. P. L. Yubero, E. Martín-Forero, J. R. Castón, D. Reguera, D. Luque, P. J. de Pablo, J. M. Rodríguez, Biophysical properties of single rotavirus particles account for the functions of protein shells in a multilayered virus. *eLife* **7**, e37295 (2018).
26. M. Radiom, T. Keys, Y. Turgay, A. Ali, S. Peret, S. Chesnov, V. Lutz-Bueno, E. Slack, R. Mezzenga, Mechanical tuning of virus-like particles. *Journal of Colloid and Interface Science* **634**, 963-971 (2023).
27. C. Zeng, L. Scott, A. Malyutin, R. Zandi, P. Van der Schoot, B. Dragnea, Virus Mechanics under Molecular Crowding. *The Journal of Physical Chemistry B* **125**, 1790-1798 (2021).
28. M. Cantero, D. Carlero, F. J. Chichón, J. Martín-Benito, P. J. De Pablo, Monitoring SARS-CoV-2 Surrogate TGEV Individual Virions Structure Survival under Harsh Physicochemical Environments. *Cells* **11**, (2022).
29. C. R. O'Riordan, A. Lachapelle, C. Delgado, V. Parkes, S. C. Wadsworth, A. E. Smith, G. E. Francis, PEGylation of adenovirus with retention of infectivity and protection from neutralizing antibody in vitro and in vivo. *Hum Gene Ther* **10**, 1349-1358 (1999).
30. M. A. Croyle, N. Chirmule, Y. Zhang, J. M. Wilson, PEGylation of E1-deleted adenovirus vectors allows significant gene expression on readministration to liver. *Hum Gene Ther* **13**, 1887-1900 (2002).
31. M. A. Croyle, N. Chirmule, Y. Zhang, J. M. Wilson, "Stealth" adenoviruses blunt cell-mediated and humoral immune responses against the virus and allow for significant gene expression upon readministration in the lung. *J Virol* **75**, 4792-4801 (2001).
32. E. A. Weaver, M. A. Barry, Effects of shielding adenoviral vectors with polyethylene glycol on vector-specific and vaccine-mediated immune responses. *Hum Gene Ther* **19**, 1369-1382 (2008).
33. T. Shimizu, M. Ichihara, Y. Yoshioka, T. Ishida, S. Nakagawa, H. Kiwada, Intravenous administration of polyethylene glycol-coated (PEGylated) proteins and PEGylated adenovirus elicits an anti-PEG immunoglobulin M response. *Biol Pharm Bull* **35**, 1336-1342 (2012).
34. K. L. Lee, S. Shukla, M. Wu, N. R. Ayat, C. E. El Sanadi, A. M. Wen, J. F. Edelbrock, J. K. Pokorski, U. Commandeur, G. R. Dubyak, N. F. Steinmetz, Stealth filaments: Polymer chain length and conformation affect the in vivo fate of PEGylated potato virus X. *Acta Biomater* **19**, 166-179 (2015).

35. Y. Eto, Y. Yoshioka, T. Ishida, X. Yao, T. Morishige, S. Narimatsu, H. Mizuguchi, Y. Mukai, N. Okada, H. Kiwada, S. Nakagawa, Optimized PEGylated adenovirus vector reduces the anti-vector humoral immune response against adenovirus and induces a therapeutic effect against metastatic lung cancer. *Biol Pharm Bull* **33**, 1540-1544 (2010).
36. P. W. Lee, S. A. Isarov, J. D. Wallat, S. K. Molugu, S. Shukla, J. E. Sun, J. Zhang, Y. Zheng, M. Lucius Dougherty, D. Konkolewicz, P. L. Stewart, N. F. Steinmetz, M. J. Hore, J. K. Pokorski, Polymer Structure and Conformation Alter the Antigenicity of Virus-like Particle-Polymer Conjugates. *J Am Chem Soc* **139**, 3312-3315 (2017).
37. S. N. Crooke, J. Zheng, M. S. Ganewatta, S. M. Guldberg, T. M. Reineke, M. G. Finn, Immunological Properties of Protein–Polymer Nanoparticles. *ACS Applied Bio Materials* **2**, 93-103 (2019).
38. J. D. Lewis, G. Destito, A. Zijlstra, M. J. Gonzalez, J. P. Quigley, M. Manchester, H. Stuhlmann, Viral nanoparticles as tools for intravital vascular imaging. *Nature Medicine* **12**, 354-360 (2006).
39. G. Destito, R. Yeh, C. S. Rae, M. G. Finn, M. Manchester, Folic Acid-Mediated Targeting of Cowpea Mosaic Virus Particles to Tumor Cells. *Chemistry & Biology* **14**, 1152-1162 (2007).
40. A. C. Tissot, R. Renhofa, N. Schmitz, I. Cielens, E. Meijerink, V. Ose, G. T. Jennings, P. Saudan, P. Pumpens, M. F. Bachmann, Versatile Virus-Like Particle Carrier for Epitope Based Vaccines. *PLOS ONE* **5**, e9809 (2010).
41. X. Liu, X. Chang, D. Rothen, M. Derveni, P. Krenger, S. Roongta, E. Wright, M. Vogel, K. Tars, M. O. Mohsen, M. F. Bachmann, AP205 VLPs Based on Dimerized Capsid Proteins Accommodate RBM Domain of SARS-CoV-2 and Serve as an Attractive Vaccine Candidate. *Vaccines* **9**, 403 (2021).
42. M. Shishovs, J. Rumnieks, C. Diebolder, K. Jaudzems, L. B. Andreas, J. Stanek, A. Kazaks, S. Kotelovica, I. Akopjana, G. Pintacuda, R. I. Koning, K. Tars, Structure of AP205 Coat Protein Reveals Circular Permutation in ssRNA Bacteriophages. *Journal of Molecular Biology* **428**, 4267-4279 (2016).
43. B. M. Chen, Y. C. Su, C. J. Chang, P. A. Burnouf, K. H. Chuang, C. H. Chen, T. L. Cheng, Y. T. Chen, J. Y. Wu, S. R. Roffler, Measurement of Pre-Existing IgG and IgM Antibodies against Polyethylene Glycol in Healthy Individuals. *Anal Chem* **88**, 10661-10666 (2016).
44. Y. C. Hsieh, H. E. Wang, W. W. Lin, S. R. Roffler, T. C. Cheng, Y. C. Su, J. J. Li, C. C. Chen, C. H. Huang, B. M. Chen, J. Y. Wang, T. L. Cheng, F. M. Chen, Pre-existing anti-polyethylene glycol antibody reduces the therapeutic efficacy and pharmacokinetics of PEGylated liposomes. *Theranostics* **8**, 3164-3175 (2018).
45. W. Humphrey, A. Dalke, K. Schulten, VMD: Visual molecular dynamics (http://www.ks.uiuc.edu/Research/vmd/). *Journal of Molecular Graphics* **14**, 33-38 (1996).
46. D. Thirumalai, B. Y. Ha, "Statistical mechanics of semiflexible chains: pA mean field variational approach" in *Theoretical and mathematical models in polymer research,* A. Grosberg, Ed. (Academic Press: San Diego, 1998).
47. Y. Pan, F. Zhang, L. Zhang, S. Liu, M. Cai, Y. Shan, X. Wang, H. Wang, H. Wang, The Process of Wrapping Virus Revealed by a Force Tracing Technique and Simulations. *Advanced Science* **4**, 1600489 (2017).
48. T. Wiegand, M. Fratini, F. Frey, K. Yserentant, Y. Liu, E. Weber, K. Galior, J. Ohmes, F. Braun, D.-P. Herten, S. Boulant, U. S. Schwarz, K. Salaita, E. A. Cavalcanti-Adam, J. P. Spatz, Forces during cellular uptake of viruses and nanoparticles at the ventral side. *Nature Communications* **11**, 32 (2020).
49. Q. Zhang, F. Tian, F. Wang, Z. Guo, M. Cai, H. Xu, H. Wang, G. Yang, X. Shi, Y. Shan, Z. Cui, Entry Dynamics of Single Ebola Virus Revealed by Force Tracing. *ACS Nano* **14**, 7046-7054 (2020).
50. J. Zhang, Y. Huang, M. Sun, T. Song, S. Wan, C. Yang, Y. Song, Mechanosensing view of SARS-CoV-2 infection by a DNA nano-assembly. *Cell Rep Phys Sci* **3**, 101048 (2022).
51. S. Li, Y. Pan, H. Teng, Y. Shan, G. Yang, H. Wang, Revealing the Cell Entry Dynamic Mechanism of Single Rabies Virus Particle. *Chem Res Chin Univ* **38**, 838-842 (2022).

52. K. M. Spillane, P. Tolar, B cell antigen extraction is regulated by physical properties of antigen-presenting cells. *Journal of Cell Biology* **216**, 217-230 (2017).
53. D. B. Hill, V. Swaminathan, A. Estes, J. Cribb, E. T. O'Brien, C. W. Davis, R. Superfine, Force generation and dynamics of individual cilia under external loading. *Biophys J* **98**, 57-66 (2010).
54. L. D. Landau, E. M. Lifshitz, A. M. Kosevich, L. P. Pitaevskii, *Theory of Elasticity: Volume 7* (Elsevier, 1986), vol. 7.
55. M. P. Neubauer, M. Poehlmann, A. Fery, Microcapsule mechanics: From stability to function. *Advances in Colloid and Interface Science* **207**, 65-80 (2014).
56. M. Buenemann, P. Lenz, Elastic properties and mechanical stability of chiral and filled viral capsids. *Physical Review E* **78**, 051924 (2008).
57. L. Menou, Y. C. Salas, L. Lecoq, A. Salvetti, C. F. Moskalenko, M. Castelnovo, Stiffness heterogeneity of small viral capsids. *Physical Review E* **104**, 064408 (2021).
58. M. Buenemann, P. Lenz, Mechanical limits of viral capsids. *Proceedings of the National Academy of Sciences* **104**, 9925-9930 (2007).
59. Z. L. Luo, B. Zhang, H. J. Qian, Z. Y. Lu, S. X. Cui, Effect of the size of solvent molecules on the single-chain mechanics of poly(ethylene glycol): implications on a novel design of a molecular motor. *Nanoscale* **8**, 17820-17827 (2016).
60. J. Kirch, A. Schneider, B. Abou, A. Hopf, U. F. Schaefer, M. Schneider, C. Schall, C. Wagner, C.-M. Lehr, Optical tweezers reveal relationship between microstructure and nanoparticle penetration of pulmonary mucus. *Proceedings of the National Academy of Sciences* **109**, 18355-18360 (2012).
61. M. Radiom, R. Hénault, S. Mani, A. G. Iankovski, X. Norel, J.-F. Berret, Magnetic wire active microrheology of human respiratory mucus. *Soft Matter* **17**, 7585-7595 (2021).
62. R. Bansil, B. S. Turner, The biology of mucus: composition, synthesis and organization. *Advanced Drug Delivery Reviews* **124**, 3-15 (2018).
63. X. M. Bustamante-Marin, L. E. Ostrowski, Cilia and mucociliary clearance. *Cold Spring Harbor perspectives in biology* **9**, (2017).
64. Y. Y. Wang, S. K. Lai, J. S. Suk, A. Pace, R. Cone, J. Hanes, Addressing the PEG mucoadhesivity paradox to engineer nanoparticles that "slip" through the human mucus barrier. *Angew Chem Int Ed Engl* **47**, 9726-9729 (2008).
65. C. S. Schneider, Q. Xu, N. J. Boylan, J. Chisholm, B. C. Tang, B. S. Schuster, A. Henning, L. M. Ensign, E. Lee, P. Adstamongkonkul, B. W. Simons, S. S. Wang, X. Gong, T. Yu, M. P. Boyle, J. S. Suk, J. Hanes, Nanoparticles that do not adhere to mucus provide uniform and long-lasting drug delivery to airways following inhalation. *Sci Adv* **3**, e1601556 (2017).
66. J. T. Huckaby, S. K. Lai, PEGylation for enhancing nanoparticle diffusion in mucus. *Advanced Drug Delivery Reviews* **124**, 125-139 (2018).
67. M.-K. Khelloufi, E. Loiseau, M. Jaeger, N. Molinari, P. Chanez, D. Gras, A. Viallat, Spatiotemporal organization of cilia drives multiscale mucus swirls in model human bronchial epithelium. *Scientific Reports* **8**, 2447 (2018).
68. P. W. Clapp, K. S. Lavrich, C. A. v. Heusden, E. R. Lazarowski, J. L. Carson, I. Jaspers, Cinnamaldehyde in flavored e-cigarette liquids temporarily suppresses bronchial epithelial cell ciliary motility by dysregulation of mitochondrial function. *American Journal of Physiology-Lung Cellular and Molecular Physiology* **316**, L470-L486 (2019).
69. X. Yao, C. Qi, C. Sun, F. Huo, X. Jiang, Poly(ethylene glycol) alternatives in biomedical applications. *Nano Today* **48**, 101738 (2023).
70. Y. Ju, J. M. Carreño, V. Simon, K. Dawson, F. Krammer, S. J. Kent, Impact of anti-PEG antibodies induced by SARS-CoV-2 mRNA vaccines. *Nature Reviews Immunology* **23**, 135-136 (2023).
71. D. Shi, D. Beasock, A. Fessler, J. Szebeni, J. Y. Ljubimova, K. A. Afonin, M. A. Dobrovolskaia, To PEGylate or not to PEGylate: Immunological properties of nanomedicine's most popular component, polyethylene glycol and its alternatives. *Adv Drug Deliv Rev* **180**, 114079 (2022).
72. B. M. Chen, T. L. Cheng, S. R. Roffler, Polyethylene Glycol Immunogenicity: Theoretical, Clinical, and Practical Aspects of Anti-Polyethylene Glycol Antibodies. *ACS Nano* **15**, 14022-14048 (2021).

73. K. Knop, R. Hoogenboom, D. Fischer, U. S. Schubert, Poly(ethylene glycol) in Drug Delivery: Pros and Cons as Well as Potential Alternatives. *Angewandte Chemie International Edition* **49**, 6288-6308 (2010).
74. "Immunogenicity Assessment for Therapeutic Protein Products" (U.S. Department of Health and Human Services, Food and Drug Administration, 2014).
75. L. Klimek, T. Kündig, M. F. Kramer, S. Guethoff, E. Jensen-Jarolim, C. B. Schmidt-Weber, O. Palomares, M. O. Mohsen, T. Jakob, M. Bachmann, Virus-like particles (VLP) in prophylaxis and immunotherapy of allergic diseases. *Allergo Journal International* **27**, 245-255 (2018).
76. Y. H. Wijesundara, F. C. Herbert, S. Kumari, T. Howlett, S. Koirala, O. Trashi, I. Trashi, N. M. Al-Kharji, J. J. Gassensmith, Rip it, stitch it, click it: A Chemist's guide to VLP manipulation. *Virology* **577**, 105-123 (2022).
77. S. Nooraei, H. Bahrulolum, Z. S. Hoseini, C. Katalani, A. Hajizade, A. J. Easton, G. Ahmadian, Virus-like particles: preparation, immunogenicity and their roles as nanovaccines and drug nanocarriers. *Journal of Nanobiotechnology* **19**, 59 (2021).
78. A. Armanious, R. Mezzenga, A Roadmap for Building Waterborne Virus Traps. *JACS Au* **2**, 2205-2221 (2022).
79. H. Matsui, B. R. Grubb, R. Tarran, S. H. Randell, J. T. Gatzy, C. W. Davis, R. C. Boucher, Evidence for periciliary liquid layer depletion, not abnormal ion composition, in the pathogenesis of cystic fibrosis airways disease. *Cell* **95**, 1005-1015 (1998).
80. S. S. Olmsted, J. L. Padgett, A. I. Yudin, K. J. Whaley, T. R. Moench, R. A. Cone, Diffusion of Macromolecules and Virus-Like Particles in Human Cervical Mucus. *Biophysical Journal* **81**, 1930-1937 (2001).
81. M. Abdulkarim, N. Agulló, B. Cattoz, P. Griffiths, A. Bernkop-Schnürch, S. G. Borros, M. Gumbleton, Nanoparticle diffusion within intestinal mucus: Three-dimensional response analysis dissecting the impact of particle surface charge, size and heterogeneity across polyelectrolyte, pegylated and viral particles. *European Journal of Pharmaceutics and Biopharmaceutics* **97**, 230-238 (2015).
82. G. A. Duncan, N. Kim, Y. Colon-Cortes, J. Rodriguez, M. Mazur, S. E. Birket, S. M. Rowe, N. E. West, A. Livraghi-Butrico, R. C. Boucher, J. Hanes, G. Aslanidi, J. S. Suk, An Adeno-Associated Viral Vector Capable of Penetrating the Mucus Barrier to Inhaled Gene Therapy. *Mol Ther Methods Clin Dev* **9**, 296-304 (2018).
83. R. A. Cone, Barrier properties of mucus. *Adv Drug Deliv Rev* **61**, 75-85 (2009).
84. D. B. Lima, T. B. de Lima, T. S. Balbuena, A. G. C. Neves-Ferreira, V. C. Barbosa, F. C. Gozzo, P. C. Carvalho, SIM-XL: A powerful and user-friendly tool for peptide cross-linking analysis. *Journal of Proteomics* **129**, 51-55 (2015).
85. H. J. Butt, B. Cappella, M. Kappl, Force measurements with the atomic force microscope: Technique, interpretation and applications. *Surface Science Reports* **59**, 1-152 (2005).
86. D. Nečas, P. Klapetek, Gwyddion: an open-source software for SPM data analysis. *Open Physics* **10**, 181-188 (2012).